International Journal of Heat and Mass Transfer 260 (2026) 128419

Contents lists available at ScienceDirect

International Journal of Heat and Mass Transfer

journal homepage: www.elsevier.com/locate/ijhmt

Thermal-hydraulic performance assessment of a micro shell-and-tube heat exchanger operating under part-load conditions in the NET Power cycle recuperator

Iván Velázquez [a,*], Frederiek Demeyer [b], Miriam Reyes [a]

[a] *Department of Energy and Fluid Mechanics Engineering, University of Valladolid, Paseo del Cauce 59, 47011 Valladolid, Spain*
[b] *Department of Mechanics & Thermal Processes, Engie R&I (Laborelec), Rodestraat 125, 1630 Linkebeek, Belgium*

ARTICLE INFO

Keywords:
Net Power cycle
Oxy-combustion
Microtube heat exchanger
Supercritical carbon dioxide
Heat transfer

ABSTRACT

This paper numerically investigates the thermal-hydraulic performance of a micro shell-and-tube heat exchanger (MSTHE) for application in the thermal recuperator of the innovative oxy-combustion-based NET Power cycle, operating under cycle-relevant part-load conditions. The aim is to support the technological transition from the established printed circuit heat exchangers (PCHE) to MSTHE, which offer a lower inertia, cost-effective, and maintenance-friendly high-performance alternative. To this end, a thermal-hydraulic computational model of the MSTHE was developed, capable of capturing the rapid variation of the supercritical CO_2 ($scCO_2$) properties and the partial filmwise condensation of the turbine exhaust gases. Results show that the MSTHE must contain at least 60,000 tubes so that the pressure drop on the tube-side is lower than 1 bar at nominal conditions. The MSTHE effectiveness decreases from 89.2% to 65.1% as the cycle load is reduced from 100% to 20%. The overall heat transfer coefficient decreases gradually between 100% and 40% cycle load, drops sharply between 40% and 30%, and then stabilizes between 30% and 20% cycle load. This stabilization is attributed to the abrupt local increase of the heat capacity on the $scCO_2$-side during the pseudo-critical phase transition, which also enhances local condensation heat release and thickens the condensate film on the shell-side. However, it was found that this phenomenon induces strong axial temperature gradients that may induce thermal stresses, representing a trade-off to the proposed compact design. While the floating microtube bundle of MSTHEs can accommodate these thermal stresses, the rigid compact block structure of PCHE is more prone to damage, revealing an additional key advantage of MSTHEs.

1. Introduction

Anthropogenic greenhouse gas emissions, primarily from fossil fuel combustion in the energy sector, which accounted for around 87 % of global emissions in 2023, have led to unprecedented atmospheric concentrations of CO_2, CH_4 and NO_x [1]. To limit the resulting increment in the Earth's surface temperature to 1.5 °C by 2050, global emissions must be reduced by 5 to 10 gigatons annually [2]. However, the use of fossil fuels is expected to continue in the medium term due to their economic relevance and widespread availability, including coal, with a demand of 167.1 exajoules in 2023 [3]. In this context, carbon capture, usage and storage (CCUS) systems, among which oxy-combustion is particularly promising [4,5], are emerging as key technologies to mitigate the environmental impact.

Oxy-combustion consists of burning fuel with pure O_2 at near stoichiometric conditions, and recirculate the flue gases (mainly CO_2 and vapor) to moderate the combustion temperature [6]. Several oxy-combustion-based power cycle configurations have been proposed, among which the NET Power cycle is considered the most promising, offering high efficiency (55.1 %) and lower plant cost (1560 € kW^{-1}) [7,8]. A thorough review of the state of art on the NET Power cycle can be found in Ref. [9].

The process flow diagram of the most up-to-date NET Power cycle embodiment is shown in Fig. 1. Under nominal high-efficiency conditions [10], natural gas is oxy-combusted with 3 % excess O_2 and moderated by a supercritical CO_2 ($scCO_2$) recirculation stream (RE-7), producing CO_2 and steam at 1104 °C and 274 bar (FG-1). The gases are expanded in a cooled turbine to 44.8 bar, while generating power. The exhaust (FG-2) is cooled in a recuperative heat exchanger (RHE),

---

* Corresponding author.
E-mail address: ivan.velazquez@uva.es (I. Velázquez).

https://doi.org/10.1016/j.ijheatmasstransfer.2026.128419
Received 25 November 2025; Received in revised form 9 January 2026; Accepted 20 January 2026
Available online 28 January 2026

Nomenclature

A_c	cross-sectional area of the tube wall, m^2
CMF	corrected mass flow
c_p	specific heat at constant pressure, $J\ kg^{-1}\ K^{-1}$
D	diameter, mm
D_e	equivalent diameter, mm
E_T	Ackermann correction factor
f	friction factor
F	flow parameter
G	mass flux, $kg\ m^{-2}\ s^{-1}$
g	gravitational acceleration, $m\ s^{-2}$
h	specific enthalpy, $J\ kg^{-1}$
$\hat{h}$	molar enthalpy, $J\ mol^{-1}$
H	pump head, m
$\Delta\hat{h}_v$	molar evaporation enthalpy, $J\ mol^{-1}$
k	iteration counter
k_{ij}	binary interaction parameter
L	heat exchanger length, mm
$\mathscr{L}$	characteristic length of the film flow, m
Le	Lewis number
$\dot{m}$	mass flow rate, $kg\ s^{-1}$
M	molecular mass, $g\ mol^{-1}$
$\dot{N}$	molar flow rate, $mol\ s^{-1}$
$\dot{n}$	local condensing molar flux, $mol\ m^{-2}\ s^{-1}$
N_s	number of sections
N_t	number of tubes
Nu	Nusselt number
p	pressure, bar
p_{cr}	critical pressure, bar
Pr	Prandtl number
P_t	pitch
$\dot{q}$	heat flux, $kW\ m^{-2}$
$\dot{Q}$	heat flow, MW
r	radius, mm
Re	Reynolds number
R_g	gas constant, $kJ\ kg^{-1}\ K^{-1}$
Ri	Richardson number
T	temperature, °C
t	thickness, mm
v	kinematic viscosity, $m^2\ s^{-1}$
$\dot{V}$	volumetric flow rate, $m^3\ s^{-1}$
x	axial direction, mm
$\hat{x}$	molar fraction in the liquid phase
$\mathscr{X}$	binary diffusion coefficient, $m^2\ s^{-1}$
$\hat{y}$	molar fraction in the gas phase

Greek letters

α	convective heat transfer coefficient, $kW\ m^{-2}\ K^{-1}$
β	pressure ratio
δ	film thickness, µm
ε	thermal effectiveness, %
ϵ	intermittency factor
η	isentropic efficiency
θ	mass transfer coefficient, $m\ s^{-1}$
ϑ	volumetric vapor content
λ	thermal conductivity, $W\ m^{-1}\ K^{-1}$
μ	dynamic viscosity, Pa s
ρ	mass density, $kg\ m^{-3}$
$\hat{\rho}$	molar density, $mol\ m^{-3}$
ς	angle of the compressor inlet guide vanes, %
τ	shear stress, MPa
υ	specific volume, $m^3\ kg^{-1}$
ω	acentric factor

Subscripts

1	H_2O
2	CO_2
b	bulk
c	cold
f	film
h	hot
i	inner
lam	laminar
o	outer
off	off-design
on	on-design
r	relative
s	shell
sat	saturation
t	tube
tur	turbulent
w	wall

Superscripts

–	mean quantity
*	guessed quantity
ˆ	molar quantity
id	ideal
in	inlet
out	outlet

Acronyms

ASU	air separation unit
CCUS	carbon capture, usage and storage
EoS	equation of state
HTS	high-temperature section
LKP	Lee-Kesler-Plöcker
LTS	low-temperature section
MSTHE	micro shell-and-tube heat exchanger
MTS	medium-temperature section
PCHE	printed circuit heat exchanger
RE	relative error
RHE	recuperative heat exchanger
$scCO_2$	supercritical CO_2

condensing steam (FG-4) and preheating recirculating streams. Part of the H_2O-depleted gas is sequestered, while the rest (RE-1) is compressed in four stages to 80 bar [11], then cooled below the pseudo-critical temperature of CO_2 (∼ 31 °C), forming a dense supercritical phase (RE-2). This enables efficient pumping in two stages: first to 120 bar (RE-4), then to 280 bar. At 120 bar, 13.34 % [12] is mixed with high-purity O_2 from the air separation unit (ASU), forming the oxidizing stream OX-1, and the remainder (RE-5) moderates combustion (RE-6) and cools the turbine (TC-1).

The favorable thermo-physical properties of the dense $scCO_2$-rich recirculating fluid lead to a low specific pumping work, which allows achieving a high optimum cycle efficiency of 55.9 % [10]. In order to pump in the dense supercritical regime, it is necessary to cool the hot turbine exhaust gases (FG-2) from 765 °C to approximately 57 °C in the RHE. This process involves an exceptionally high enthalpy change within the RHE, which demands a considerable heat transfer surface. Consequently, as shown in Fig. 1, the RHE is divided into three (or even more [9]) consecutive heat exchange sections: low-temperature section

(LTS), medium-temperature section (MTS), and high-temperature section (HTS). Moreover, to compensate for the difference between the heat capacities of the pressurized recirculation stream and the exhaust stream [13], Fig. 1 illustrates the application of additional heat of compression in the RHE, coming from both the ASU and the adiabatic compression of 11.4 % [10] of the exhaust gases, extracted after the MTS at 138 °C (slightly above the dew point) [14,15], in the BPC compressor.

To cope with the demanding high heat transfer conditions within the RHE, printed circuit heat exchangers (PCHE) have become the predominant technology [16,17]. In fact, the 50 MW_{th} NET Power cycle demonstration pilot plant uses PCHEs consisting of etched 1.6 mm zigzag channels for the RHE [18]. However, recent advances in compact heat exchangers [19,20] have revealed multiple advantages of innovative micro shell-and-tube heat exchangers (MSTHE) over PCHEs: (i) they offer greater compactness, resulting in lower mass, cost, and thermal inertia; (ii) they are easier to clean and maintain against corrosion clogging issues [21–23], as MSTHEs can be easily disassembled, while PCHEs must be destroyed to inspect the interior; (iii) their manufacturing process is more cost-effective, as it is inherited from conventional shell-and-tube heat exchangers. The lower thermal inertia of MSTHEs is particularly relevant for the proper operation of the NET Power cycle in the context of the European electricity market, which is characterized by its high variability degree.

In the context of the NET Power cycle, no studies have yet been reported in literature addressing the application of MSTHEs in the RHE. However, several research efforts have been conducted on their implementation in the recuperator of closed scCO_2 Brayton cycles. Jiang et al. [20] optimized the number of tubes, tube diameter, and tube pitch, in a baffle-free MSTHE bundle, and compared its thermal-hydraulic performance to a PCHE under steady and dynamic conditions. The MSTHE showed higher heat transfer coefficients, requiring less heat exchange area and metal mass, and demonstrated superior surface area density and faster dynamic response. Kwon et al. [19] confirmed these results, reporting surface area densities of up to 2500 $\text{m}^2\ \text{m}^{-3}$ for PCHEs and up to 4500 $\text{m}^2\ \text{m}^{-3}$ for MSTHEs with 1 mm tubes. Thar energy developed a prototype MSTHE with ∼ 20,000 microtubes in a single shell, using Inconel 625 on the hot-side and SS316L on the cold-side, and designed a single-flange asymmetric pressure vessel to improve structural integrity and reduce manufacturing costs [24].

Cai et al. [25] numerically investigated the heat transfer characteristics between scCO_2 and water in a MSTHE with 1.6 mm tubes, where scCO_2 flowed at low Reynolds numbers and was cooled by shell-side water. They found that the scCO_2 heat transfer coefficient increases with CO_2 mass flow, but is unaffected by the water flow rate. Counterflow arrangement yielded higher performance than crossflow. However, experiments conducted by Cai et al. [26] on a 37 tube MSTHE (1.6 mm diameter, 500 mm length) revealed that shell-side baffles improve heat transfer, with smaller baffle spacing further enhancing performance, although this also resulted in an increased pressure drop [27]. This apparent discrepancy may be attributed to the dominance of buoyancy forces at low Reynolds numbers, where a crossflow pattern can induce thermal stratification in the scCO_2-side and suppress turbulence quantities.

Jin et al. [28] conducted over forty experimental series to investigate the thermal-hydraulic performance in a fabricated five-cell MSTHE using scCO_2 and air as working fluids, with the Reynolds number ranging between 9000 to 17,000 and 2000 to 18,000, respectively. The experimental outcomes were used to validate the thermal-hydraulic models and correlations employed by [29,30]. The results showed good agreement with model predictions, reporting deviations within 10 % for all key performance metrics, including thermal conductance and pressure drop.

Despite the growing interest in the MSTHE architecture, the available literature remains limited and is restricted to a few studies applied

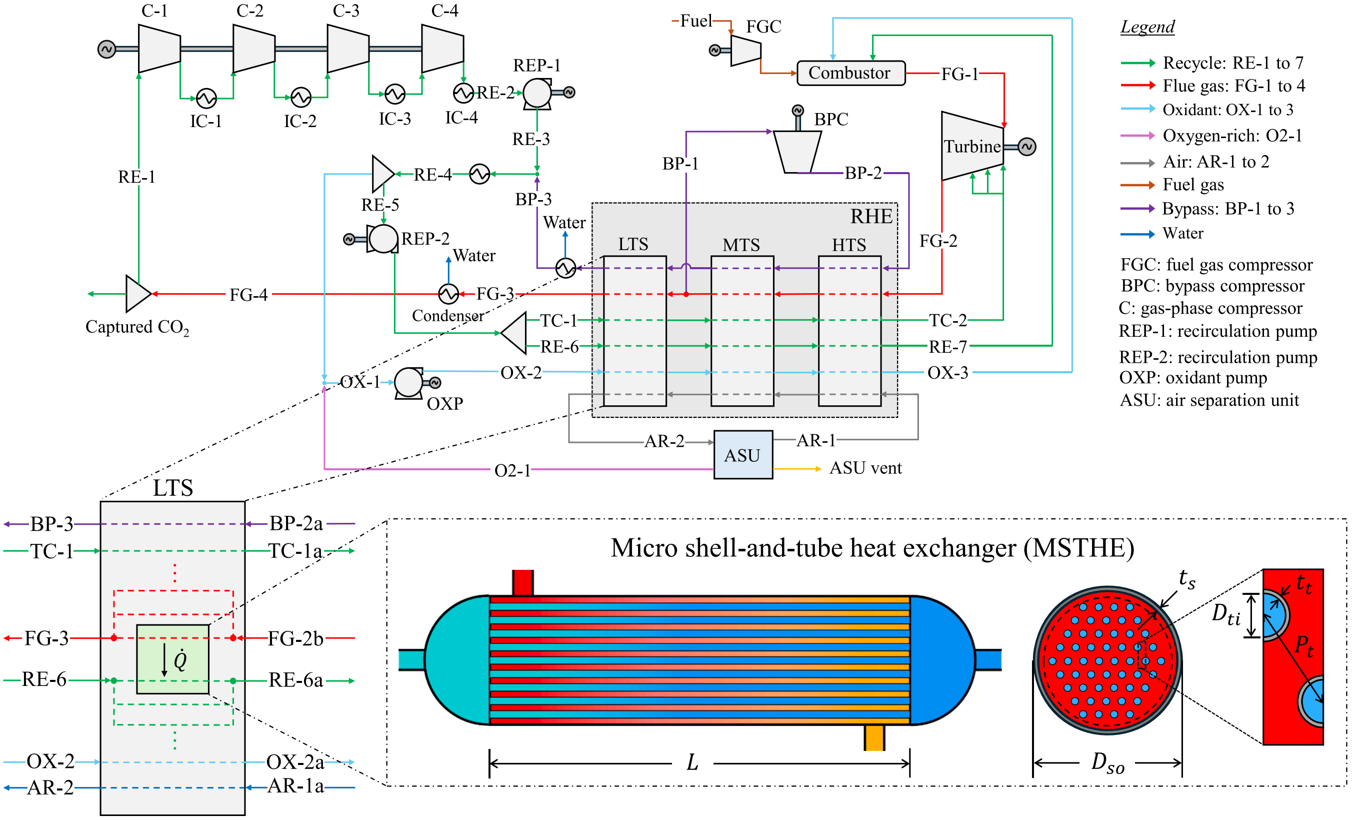

Fig. 1. Process flow diagram of the oxy-combustion-based NET Power cycle [10,14], and MSTHE configuration and location within the low temperature section (LTS) of the recuperative heat exchanger (RHE).

to $scCO_2$ Brayton cycles, mainly focused on geometric design and on the numerical and experimental analysis on heat transfer and pressure drop. Regarding the NET Power cycle, no previous studies have investigated the thermal-hydraulic behavior of MSTHEs under the unique operating conditions of the recuperator, which involves partial-load regimes and the presence of hot-gas condensation phenomena. This lack of studies represents a research gap that this paper addresses through the following contributions:

i. A numerical evaluation of the performance of a MSTHE in the NET Power cycle recuperator under cycle-relevant part-load conditions.
ii. A sensitivity analysis of the thermal-hydraulic behavior of the MSTHE as a function of key geometric design variables.

Findings form this study provide a valuable theoretical background that can serve as a basis for the efficient design of MSTHE units for application in the NET Power cycle. It is worth noting that, as illustrated in Fig. 1, this study focuses on an MSTHE located in the low-temperature section, where heat is exchanged between the $scCO_2$-rich recirculating stream (RE-6) flowing through the microtubes, and the wet turbine exhaust gases (FG-2) flowing through the shell-side. Prioritizing the low-temperature section is justified by the following two reasons:

i. RE-6, primarily composed of $scCO_2$, operates near the pseudo-critical region in the low-temperature section, where rapid thermophysical property variations significantly influence heat transfer.
ii. FG-2 reaches saturation conditions in the low-temperature section, forming a condensing H_2O-rich film around the tubes, which influences heat transfer effectiveness.

These two reasons introduce an additional challenge in the thermal-hydraulic design of MTHE units. This challenge is not found in the medium- and high-temperature sections, which operate far from the pseudo-critical region and sensible heat exchange between ideal-like gases can be tackled on the basis of conventional constant-property flows.

To carry out the present study, a thermal-hydraulic computational model of the MSTHE, incorporating partial filmwise condensation, was developed as described in Section 2. Results are presented in Section 3, with the main conclusions and findings summarized in Section 4.

2. Micro shell-and-tube heat exchanger modeling approach

The off-design modeling approach of the MSTHE for application in the condensative low-temperature section of the NET Power cycle recuperator is presented in this section. The operating conditions are presented in Section 2.1. The geometric parameters of the MSTHE are described in Section 2.2. The thermal-hydraulic model, which involves the governing equations and the heat and mass transport theorems, is detailed in Section 2.3. Finally, the numerical procedures and discretization strategy are presented in Sections 2.4 and 2.5.

2.1. Operating conditions

Before discussing the MSTHE performance, it is necessary to establish the part-load operating conditions of the NET Power cycle. These operating parameters define the boundary conditions applied in the MSTHE model. To determine the off-design operating conditions, the thermodynamic model of the NET Power cycle under nominal conditions, developed in Aspen Plus V12.1 [31] by Velázquez et al. [10], was adapted to simulate the part-load operation. The off-design models of the turbine, compressors, pumps, and thermal recuperator are described in Appendix A of the supplementary materials. From a 100 % load condition, corresponding to the optimized cycle configuration [10], the cycle load degree was progressively reduced up to 20 %, in 10 % increments. For each cycle load level, mass flows, temperatures, pressures and compositions were captured at the inlet of a MSTHE located in the low-temperature section of the NET Power cycle recuperator, as depicted in Fig. 1. Table 1 shows the resulting off-design boundary conditions of the MSTHE, as a function of the cycle load level ranging from 100 % to 20 %. Subscripts "*c*" and "*h*" refer to the tube-side cold $scCO_2$ and shell-side hot $CO_2 – H_2O$ gas mixture, respectively. It is important to note that the cycle load percentage in this study was defined based on the fuel mass flow rate entering the cycle. A 100 % load corresponds to a fuel mass flow rate of 16.52 kg s^{-1}.

It can be seen in Table 1 that, with the exception of p_h^{in}, which remains constant at 44.80 bar, mass flow rates, temperatures, and pressures decrease as the cycle load is reduced. Under part-load conditions, the thermal input from fuel combustion decreases, leading to lower water formation and a reduction of $\hat{y}_{H_2O,h}^{in}$. In addition, the heat released from combustion is reduced, which would tend to lower the turbine outlet temperature. To maintain this temperature constant, which is essential for operating the RHE with high effectiveness regardless of the cycle load level, the recirculation flows are reduced. This justifies the decrease of both $\dot{m}_c$ and $\dot{m}_h$. The p_c^{in} decreases in response to the reduction of the recirculation flow, in order to comply with the turbine performance curve. Consequently, T_c^{in} decreases due to the lower fluid heating by viscous dissipation in the $scCO_2$ pumps. T_h^{in} drops as a result of the reduction of the RHE effectiveness. Although the recirculation flow contains about 2 % mol of impurities [32], pure $scCO_2$ was assumed for simplification purposes.

2.2. Baseline geometry parameters

A schematic diagram of the baseline configuration and cross-sectional view of the MSTHE are shown in Fig. 1. The MSTHE is composed by two inlet flanges, two outlet flanges, two headers, a straight single floating microtube bundle, and a perfectly insulated external shell. The floating tubesheet configuration allows axial expansion to avoid thermal loads. Since the thermal-hydraulic study of the MSTHE was focused on the low-temperature section of the recuperator, the components are fabricated from SS316L [22,23]. Unlike conventional shell-and-tube heat exchangers, the MSTHE does not employ flow-guiding baffles. The counterflow arrangement enables high heat transfer rates and avoids the pressure drop associated with baffles [13]. The shell-side fluid enters and exits the exchanger perpendicular to the microtube bundle. It then flows along the remaining annular space between the shell and the tube bundle, in a counterflow direction relative to the tube-side flow, over the length of the MSTHE.

As can be seen in Fig. 1, the key geometry parameters that characterize the MSTHE are: length of the tubes (L), number of tubes (N_t), inner diameter of the tubes (D_{ti}), tube wall thickness (t_t), outer diameter of tubes (D_{to}), distance between tubes (also known as "pitch", P_t), outer diameter of the shell (D_{so}), thickness of the shell (t_s), and inner diameter of the shell (D_{si}). Tube bundles can be arranged in either square or triangular configurations. Among these, the triangular arrangement offers higher compactness and enhanced heat transfer performance [33]. Therefore, as shown in Fig. 1, triangular tube layout was adopted in this study. Given N_t, D_{to} and P_t, the geometry of the MSTHE can be computed as proposed by Jiang et al. [34]. D_{si} is calculated by Eq. (1); where *CL* is the tube layout constant, which in this case is $\sqrt{3}/2$; *CTP* is the constant (0.93 for a single pass) that considers the residual clearance space between the outer diameter of the tube bundle (represented by a dashed line in the cross-sectional view of the MSTHE in Fig. 1) and the inner diameter of the shell.

$$D_{si} = 2P_t \left[\frac{(CL)N_t}{\pi(CTP)} \right]^{0.5} \tag{1}$$

The equivalent diameter D_e, defined as 4 x free flow area / wetted perimeter, is the characteristic dimension used to compute the

Table 1

Boundary conditions (BCs) for a 10 MW_{th} off-design MSTHE, as a function the cycle load degree based on the thermal energy of the feedstock from 100 % to 20 %.

BC	Unit	NET Power cycle part load degree (fuel-based)								
		100 %	90 %	80 %	70 %	60 %	50 %	40 %	30 %	20 %
$\dot{m}_c$	kg s^{-1}	57.71	56.21	54.31	51.94	49.01	45.39	40.92	35.31	28.10
$\dot{m}_h$	kg s^{-1}	71.44	69.58	67.23	64.29	60.66	56.19	50.65	43.72	34.78
T_c^{in}	°C	44.40	42.64	40.74	38.66	36.36	33.81	30.94	27.72	23.89
T_h^{in}	°C	138.00	136.66	135.16	133.47	131.52	129.22	126.43	122.86	117.92
p_c^{in}	bar	278.99	261.95	243.79	224.34	203.39	180.60	155.54	127.56	95.53
p_h^{in}	bar	44.80	44.80	44.80	44.80	44.80	44.80	44.80	44.80	44.80
$\widehat{y}_{H_2O,h}^{in}$	%	4.85	4.67	4.48	4.28	4.05	3.81	3.54	3.23	2.86
$\widehat{y}_{CO_2,c}^{in}$	%	100	100	100	100	100	100	100	100	100

correlations for heat transfer, Eq. (2), and pressure drop, Eq. (3), for the non-circular cross-sectional shell-side flow [35].

$$D_e = \frac{4\left(\sqrt{3}\,P_t^2/4 - \pi D_{to}^2/8\right)}{\pi D_{to}/2} \tag{2}$$

$$D_e' = \frac{4\left(\sqrt{3}\,P_t^2/4 - \pi D_{to}^2/8\right)}{(\pi D_{to} + \pi D_{si}/N_t)/2} \tag{3}$$

The thickness of the tubes and the shell were evaluated by Eqs. (4) and (5), and the tubesheet thickness was calculated by Eqs. (6) and (7) employing the 11th TEMA Standard [36]. p_d is the design pressure; t_e, E, S, and Y are mechanical design parameters, for which values are shown in Table 2; $F_{ts} = 1$ for fixed and floating tubesheet; and k_e is the mean ligament efficiency.

$$t_t = t_{et} + \frac{p_{dt} D_{to}}{2(SE + p_{dt} Y)} \tag{4}$$

$$t_s = t_{es} + \frac{p_{ds} D_{si}}{2(SE + 0.6 p_{ds})} \tag{5}$$

$$t_{ts} = \frac{F_{ts} D_{si}}{3}\left(\frac{p_d}{k_e S}\right)^{0.5} \tag{6}$$

$$k_{e,tri} = 1 - 0.907 \Big/ (P_t/D_{to})^2 \tag{7}$$

2.3. Thermal-hydraulic modeling approach

Fig. 2 presents the heat transfer model and control volumes, corresponding to the superheated and saturated regions, including the associated heat and mass fluxes, used in the derivation of the governing equations. The hot gas mixture enters the shell-side in a superheated vapor state. As it flows through the heat exchanger, the shell-side temperature, T_h, progressively decreases until the fluid in the near-wall region reaches the saturation temperature, i.e., $T_{wo} = T_{sat}$. At this point, condensation of the vapor begins, along with small traces of dissolved CO_2, forming a H_2O-rich condensation film over the cooling tube walls [39,40], as illustrated in Fig. 2. The film thickness, δ, increases along the flow direction due to the continued condensation at the vapor-liquid interface. This condensate layer introduces an additional thermal resistance. The latent heat released during condensation must be conducted through the film before reaching the outer wall of the microtubes.

Table 2

Mechanical design parameters of Eqs. (4) - (7).

	t_e (mm)	p_d (kPa)	S^* (kPa)	E	Y	Reference
Tube	0.254	$1.05 p_{c,in}$	$87.4 \cdot 10^3$	1.00	0.75	[37,38]
Shell	3.175	$p_{h,in}$+170 kPa	$87.4 \cdot 10^3$	0.85	-	[36]

[*] For a design temperature of 150 °C.

2.3.1. Model assumptions

The following assumptions were adopted in the development of the computational model:

i. Steady-state flow.
ii. Newtonian fluid behavior.
iii. Negligible changes in kinetic and potential energy.
iv. Negligible axial heat conduction in the fluid phases (i.e., convection-dominated problem). This assumption is justified despite the small hydraulic lengths, as the flow presents sufficiently high Peclet numbers. In particular, for nominal conditions, the minimum local Peclet numbers are $2.5{\cdot}10^4$ and $2.6{\cdot}10^4$ on the tube and shell sides, respectively, while at a 20 % load the values are $2.2{\cdot}10^4$ and $1.3{\cdot}10^4$.
v. The inertia forces, resulting from the high velocity of the shell gas, are sufficient to: (i) prevent condensate droplets from falling due to gravitational action, and (ii) assume a constant film thickness in the tangential direction of the tube. Therefore, δ represents the circumferential average film thickness.

The heat transfer mechanisms vary depending on whether the shell-side $CO_2 - H_2O$ mixture is superheated or saturated. Consequently, the governing heat transfer equations are formulated in differential form separately for each condition in Section 2.3.2.

2.3.2. Governing heat transfer equations

The mathematical modeling approach of the MSTHE for both the superheated ($T_{wo} > T_{sat}$) and saturated ($T_{wo} \le T_{sat}$) regions is summarized in Table 3.

The governing equations for the superheated and saturated regions were derived from the conservation of mass, chemical species and energy, applied to the left and right differential control volumes depicted in Fig. 2, respectively. The subscript 1 denotes H_2O and 2 denotes CO_2. Conservation equations in Table 3 are complemented by kinetic theorems for heat and mass transfer in Section 2.3.3.

In Eqs. (12) and (21), λ_s represents the thermal conductivity of SS316L, which was assumed to be constant and equal to 16 W m^{-1} K^{-1}. In the condensate film energy equation, expressed in Eq. (19), the molar enthalpy change of the liquid film was neglected. Hence, T_f was obtained from the iterative solution of Eq. (19). In Eqs. (13) – (21), δ was not considered to calculate the heat and mass transfer area, since it is much smaller than the outer diameter of the tubes. The energy balance expressed in Eq. (20) was used to calculate the bulk temperature of the shell-side gases, T_h, when it is above T_{sat}. Otherwise, T_h was set equal to T_{sat}. T_w was calculated by means of the wall thermal resistance network of Fig. 3 [30] by Eq. (22), where $r = (r_i + r_o)/2$. T_{wo} and T_{wi} were determined by imposing that, under steady-state conditions, the heat flow transferred by convection in the fluid phases equals the heat flow conducted through the solid wall.

$$T_w = \frac{\ln(r/r_i)T_{wo} + \ln(r_o/r)T_{wi}}{\ln(r_o/r_i)} \tag{22}$$

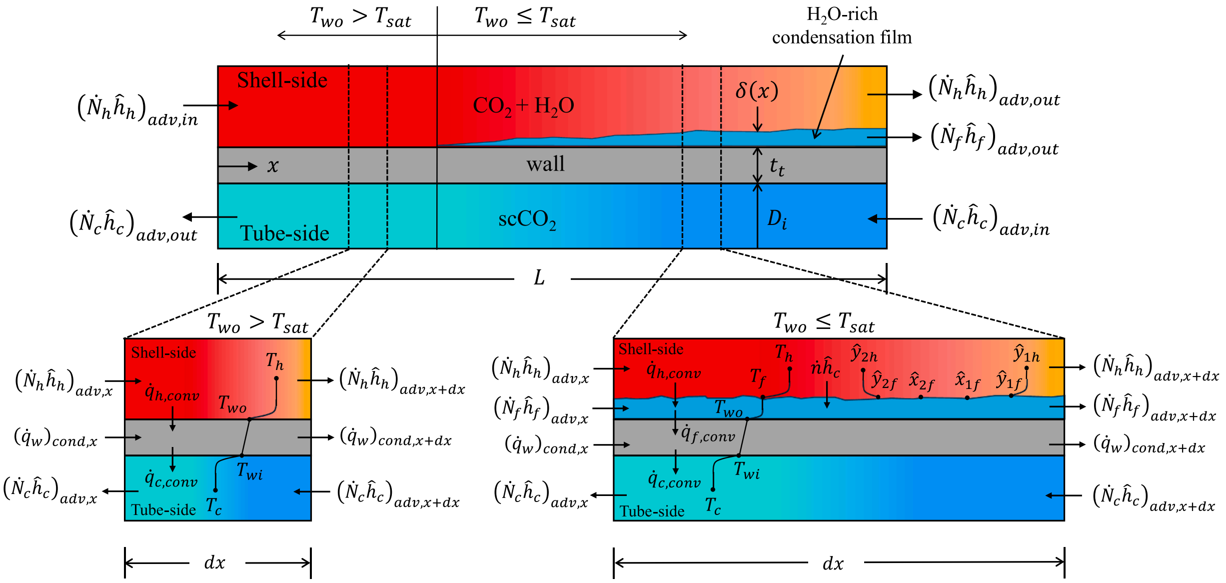

Fig. 2. Heat transfer model of the MSTHE and control volumes, including the energy and mass fluxes, for the deduction of the differential unidimensional governing equations for the superheated and saturated regions. Subscript "h" stands for hot-fluid (shell-side) and "c" for cold-fluid (tube-side). Subscript "1″ refers to H$_2$O and "2" to CO$_2$.

Table 3
Governing heat transfer equations of the MSTHE model for the superheated $T_{wo} > T_{sat}$) and saturated ($T_{wo} \leq T_{sat}$) regions.

Conservation equation	Expression	Eq.
Superheated region ($T_{wo} > T_{sat}$)		
Mass (shell-side)	$\frac{d\dot{N}_h}{dx} = 0$	(8)
Mass (tube-side)	$\frac{d\dot{N}_c}{dx} = 0$	(9)
Energy (shell-side)	$\dot{N}_h\frac{d\widehat{h}_h}{dx} = -\alpha_h N_t \pi D_{to}(T_h - T_{wo})$	(10)
Energy (tube-side)	$\dot{N}_c\frac{d\widehat{h}_c}{dx} = -\alpha_c N_t \pi D_{ti}(T_{wi} - T_c)$	(11)
Energy (solid wall)	$\lambda_s A_c\frac{d^2 T_w}{dx^2} = \alpha_c \pi D_{ti}(T_{wi} - T_c) - \alpha_h \pi D_{to}(T_h - T_{wo})$	(12)
Saturated region ($T_{wo} \leq T_{sat}$)		
Mass (tube-side)	$\frac{d\dot{N}_c}{dx} = 0$	(13)
Mass (film)	$\frac{d\dot{N}_f}{dx} = \dot{n} N_t \pi D_{to},$	(14)
Mass (shell-side)	$\frac{d\dot{N}_h}{dx} = -\dot{n} N_t \pi D_{to}.$	(15)
Chemical species (film)	$\frac{d\dot{N}_{f1}}{dx} = \dot{n}_1 N_t \pi D_{to}$	(16)
Chemical species (shell-side)	$\frac{d\dot{N}_{h1}}{dx} = -\dot{n}_1 N_t \pi D_{to}$	(17)
Energy (tube-side)	$\dot{N}_c\frac{d\widehat{h}_c}{dx} = -\alpha_c N_t \pi D_{ti}(T_{wi} - T_c)$	(18)
Energy (film)	$\dot{n} N_t \pi D_{to} \Delta\widehat{h}_v(T_f) + \alpha_h E_T N_t \pi D_{to}(T_h - T_f) - \alpha_f N_t \pi D_{to}(T_f - T_{wo}) = 0$	(19)
Energy (shell-side)	$\dot{N}_h\frac{d\widehat{h}_h}{dx} = \dot{n} N_t \pi D_{to}\overline{\widehat{c}}_{p,h}(T_h - T_f) - \alpha_h E_T N_t \pi D_{to}(T_h - T_f)$	(20)
Energy (solid wall)	$\lambda_s A_c\frac{d^2 T_w}{dx^2} = \alpha_c \pi D_{ti}(T_{wi} - T_c) - \alpha_f \pi D_{to}(T_f - T_{wo})$	(21)

Subscripts: c = tube-side cold fluid; h = shell-side hot fluid; w = wall; f = film; 1 = H$_2$O; 2 = CO$_2$.

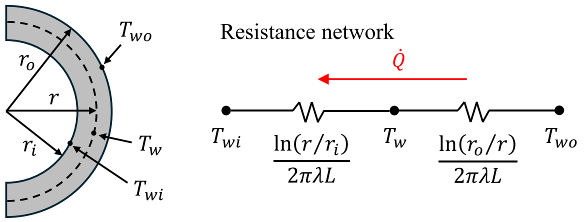

Fig. 3. Cross section of a half tube and resistance network to determine the mean tube wall temperature T_w.

The mole fraction of CO$_2$ in the H$_2$O-rich condensate phase was calculated at the vapor-liquid interface, at the temperature T_f, where thermodynamic equilibrium was assumed to occur. For vapor-liquid equilibrium calculations, a fitted virial-type Lee-Kesler-Plöcker (LKP) equation of state (EoS) was employed. The LKP EoS was fitted in Ref. [32] using experimental vapor-liquid equilibrium data for CO$_2$ – H$_2$O mixtures over a pressure and temperature ranges of 10 – 170 bar and 25 – 150 °C. The resulting binary interaction parameter between CO$_2$ and H$_2$O was $k_{ij} = 0.0125$, with $k_{ij} = k_{ji}$. The rest of fluid properties were computed using the GERG – 2008 EoS [41].

Due to the low mole fraction of CO$_2$ in the condensate film [42,43], CO$_2$ accumulates near the vapor-liquid interface, forming a concentration boundary layer that acts as a mass transfer barrier. This accumulation delays the direct contact between vapor and the condensate surface, thereby reducing the efficiency of the condensation process. Before condensation can occur, water vapor must first diffuse through this resistive gas-phase layer to reach the liquid film. Mass transport within this gas phase layer is predominantly convective. Based on the mole fraction gradients of H$_2$O and CO$_2$ in the gas phase (see Fig. 2), the local condensing molar flux was calculated using Eq. (23) [44,45].

$$\dot{n} = \widehat{\rho}_h \theta_h \ln\left(\frac{\widehat{x}_{1f} - \widehat{y}_{1f}}{\widehat{x}_{1f} - \widehat{y}_{1h}}\right), \tag{23}$$

Since mass and heat transfer occur simultaneously in the shell-side fluid phase, the Ackermann correction factor E_T [46], defined in Eq. (24), was introduced into Newton's cooling law for the shell-side convective heat transport (Eqs. (19) and (20)).

$$E_T = \frac{\phi_T}{1 - e^{-\phi_T}}, \text{ with } \phi_T = \frac{\dot{n}\widehat{c}_{p,h}}{\alpha_h}. \tag{24}$$

2.3.3. Heat and mass transfer correlations

This section presents the correlations used to calculate the heat transfer coefficients on the shell-side α_h, microtube-side α_c, and condensate film α_f, as well as the mass transfer coefficient θ_h, and the friction factors for both the shell-side f_h, and microtube-side f_c [47].

α_h was computed using forced convection correlations, which depend on whether the flow regime through the shell is laminar, turbulent or transitional:

Laminar flow regime ($Re_{D_e} < 2300$) [48]:

$$Nu_{h,b,lam} = \left[Nu^3_{h,b,lam\_1} + 0.7^3 + \left(Nu_{h,b,lam\_2} - 0.7\right)^3 + Nu^3_{h,b,lam\_3}\right]^{1/3},$$

$$Nu_{h,b,lam\_1} = 3.66,$$

$$Nu_{h,b,lam\_2} = 1.077\left(Re_{h,b,D_e} Pr_{h,b} D_e/x\right)^{1/3},$$

$$Nu_{h,b,lam\_3} = \frac{1}{2}\left(\frac{2}{1+22Pr_{h,b}}\right)^{1/6}\left(Re_{h,b,De} Pr_{h,b} D_{he}/x\right)^{1/2}. \tag{25}$$

Turbulent flow regime ($Re_{D_e} > 10^4$) [49,50]:

$$Nu_{h,b,tur} = \frac{(f_h/8)\left(Re_{h,b,D_e} - 1000\right)Pr_{h,b}}{1 + 12.7(f_h/8)^{1/2}\left(Pr^{2/3}_{h,b} - 1\right)}\left(\frac{Pr_{h,b}}{Pr_{h,w}}\right)^{0.11} C_A,$$

$$C_A = 1 + \frac{1}{3}(D_e/x)^{2/3}. \tag{26}$$

Transitional flow regime ($2300 < Re_{D_e} < 10^4$):

$$Nu_{h,b,tra} = (1-\epsilon) Nu_{h,b,lam}\big|_{Re_{h,b,D_e}=2300} + \epsilon Nu_{h,b,tur}\big|_{Re_{h,b,D_e}=10^4},$$

$$\epsilon = \frac{Re_{h,b,D_e} - 2300}{10^4 - 2300}. \tag{27}$$

Subscripts "*b*" and "*w*" refer to properties calculated at bulk and wall temperature, respectively.

α_c was calculated using the empirical correlation given in Eq. (28). This correlation was fitted from experimental measurements of heat transfer coefficients in scCO$_2$ flowing through a horizontally-oriented microtube with an inner diameter of 0.88 mm, up to 300 bar [51]. The effects of natural convection on heat transfer, arising from the steep radial density gradients in scCO$_2$ near to the critical pressure, are accounted for through the Richardson number, R_i. The range of application of Eq. (28) is: $10 \le p_c \le 30$ MPa, $4099.9 \le Re_{c,b} \le 23847.4$, $19.8 \le T_{c,b} \le 101.8$ °C and $8.3 \le \dot{q}_c \le 21.3$ kW m^{-2}.

$$Nu_{c,b} = 0.0038 Re^{0.850}_{c,b} Pr^{2.038}_{c,b} Ri^{-0.028}_{c,b}\left(\frac{\rho_{c,w}}{\rho_{c,b}}\right)^{1.518}\left(\frac{\mu_{c,w}}{\mu_{c,b}}\right)^{4.690}\left(\frac{\lambda_{c,w}}{\lambda_{c,b}}\right)^{2.556}\left(\frac{\bar{c}_{p,c}}{c_{p,c,w}}\right)^{1.943},$$

$$\bar{c}_{p,c} = \frac{h_{c,w} - h_{c,b}}{T_{c,w} - T_{c,b}}. \tag{28}$$

α_f was calculated, either for laminar or turbulent flow regimes, from the Nusselt [52] and Müller [53] correlations, respectively, as expressed in Eqs. (29) and (30). The range of application of Eq. (29) involves film Reynolds numbers up to 1800, which includes the wavy laminar regime, while Eq. (30) is applicable for Reynolds values above 1800.

$$Nu_{f,lam} = \frac{\alpha_{f,lam}\mathscr{L}}{\lambda_f} = 0.693\left(\frac{1 - \rho_h/\rho_f}{Re_f}\right)^{1/3}, \tag{29}$$

$$Nu_{f,tur} = \frac{\alpha_{f,tur}\mathscr{L}}{\lambda_f} = \frac{0.0283 Re_f^{7/24} Pr_f^{1/3}}{1 + 9.66 Re_f^{-3/8} Pr_f^{-1/6}}, \tag{30}$$

In Eqs. (29) and (30), $\mathscr{L}$ is the characteristic length of the film flow and Re_f is the film Reynolds number, defined as follows:

$$\mathscr{L} = \left(\frac{v_f^2}{g}\right)^{1/3} \tag{31}$$

$$Re_f = \frac{\dot{m}_f}{\pi D_{to} \mu_f} \tag{32}$$

Although Eqs. (29) and (30) were derived for a film flow over vertical surfaces, they can be reasonably extended to horizontal tubes [54]. Nu_f, and thus α_f, was calculated by combining $Nu_{f,lam}$ and $Nu_{f,tur}$, through the following quadratic superimposition:

$$Nu_f = \frac{\alpha_f \mathscr{L}}{\lambda_f} = \sqrt{\left(K_{f,lam} K_\tau Nu_{f,lam}\right)^2 + \left(K_{f,tur} K_\tau Nu_{f,tur}\right)^2}. \tag{33}$$

Coefficients K_τ, $K_{f,lam}$ and $K_{f,tur}$, introduced in Eq. (33), account for the influence of the shell gas flow velocity on the heat transfer within the film. At the vapor-liquid interface, the axial velocity of the film and shell gas flows must coincide [55]. This generates a velocity gradient of the shell gas in the near-interface region and, thus, a shear stress at the interface, τ_{hf}. τ_{hf} increases the mean velocity of the film flow, leading to two effects: (i) film thinning, which reduces the thermal resistance; and (ii) amplification of turbulent fluctuations in the film, which intensifies heat diffusion by turbulent action. Effect (i) is accounted for by K_τ, which is valid for laminar and turbulent flow regimes [56]. Effect (ii) is accounted for by $K_{f,lam}$ and $K_{f,tur}$, which depend on the flow regime [57]. Details on the calculation of K_τ, $K_{f,lam}$ and $K_{f,tur}$ are provided in Appendix B of the supplementary material. In addition, δ was calculated from the local volumetric vapor content, ϑ, according to Eq. (34). The calculation procedure of ϑ is also presented in Appendix B.

$$\delta = \frac{(1-\vartheta)}{4} D_{to}, \tag{34}$$

Resistance in the gas phase, caused by CO$_2$ accumulation, was taken into account based on the mass transfer coefficient θ_h. θ_h was calculated from α_h using the Chilton-Colburn analogy [58]:

$$\theta_h = \frac{\alpha_h}{\widehat{\rho}_h \widehat{c}_{p,h} Le^{0.6}}, \tag{35}$$

where the Lewis number, Le, is defined as the ratio of thermal diffusivity to mass diffusivity, $Le = \lambda_h/\left(\widehat{\rho}_h \widehat{c}_{p,h} \chi_h\right)$. The binary diffusion coefficient between CO$_2$ and H$_2$O, χ_h, was estimated using the Fuller's correlation [59], at a pressure of 1 bar, as shown in Eq. (36).

$$\chi_h{}^{id} = \frac{0.00143 T_h^{1.75}\left(M_1{}^{-1} + M_2{}^{-1}\right)^{1/2}}{p\sqrt{2}\left[\left(\sum \Delta_{\upsilon 1}\right)^{1/3} + \left(\sum \Delta_{\upsilon 2}\right)^{1/3}\right]^2},$$

$$\text{with } \Delta_{\upsilon 1} = 13.1 \text{ and } \Delta_{\upsilon 2} = 26.9. \tag{36}$$

To account for the effect of elevated pressures, $\chi_h{}^{id}$ was corrected using the Riazi-Whitson correlation [60] of Eq. (37), which depend on the critical pressure of the mixture, p_{cr}, and the acentric factor, ω.

$$\frac{(\rho_h \chi_h)}{(\rho_h \chi_h)^{id}} = 1.07\left(\frac{\mu_h}{\mu_h^{id}}\right)^{B + C\frac{p}{p_{cr}}},$$

$$\text{with } B = -0.27 - 0.38\omega \text{ and } C = -0.05 + 0.1\omega. \tag{37}$$

It is worth noting that the heat and mass transfer correlations on the shell-side can be reliably applied within their application range, since the flow is not in a supercritical state.

f_h and f_c were calculated by using the high-accuracy explicit model of Romeo et al. [61], and the temperature correction factor of Musgrove et al. [62], as follows:

$$\frac{1}{\sqrt{f_o}} = -2\ln\left(\frac{\varepsilon/D}{3.7065} - \frac{5.0272}{Re_{i,b,D_e}}\ln\left(\frac{\varepsilon/D}{3.827} - \frac{4.567}{Re_{i,b,D_e}}\ln\left(\left(\frac{\varepsilon/D}{7.7918}\right)^{0.9924} + \left(\frac{5.3326}{208.815+Re_{i,b,D_e}}\right)^{0.9345}\right)\right)\right),$$

$$f_h \text{ or } f_c = f_o\left(\frac{T_b}{T_w}\right)^{0.1}. \tag{38}$$

2.4. Numerical procedures for model resolution

The thermal-hydraulic model of the MSTHE was implemented in Matlab R2022b [63]. The numerical procedure used to solve the model is illustrated in the flow diagram shown in Fig. 4. Since heat transfer in scCO$_2$ and filmwise condensation are local phenomena, the heat exchanger length was discretized into N_s heat exchange sections. The governing differential equations for heat transfer were then solved numerically along the direction of the shell-side flow discretizing the convective transport terms of the governing equations using the first-order upwind discretization scheme [64].

The procedure begins with the input of the independent geometric parameters. Eqs. (1) – (7) are used to define the complete geometry of the MSTHE. Next, boundary conditions are specified. Due to the counterflow configuration, the boundary condition for the tube-side inlet temperature must be applied at $k = N_s$, even though the numerical integration begins at $k = 1$. Consequently, the initial temperature of the tube-side fluid at $k = 1$ must be estimated and subsequently adjusted iteratively until the calculated temperature at $k = N_s$ matches the specified boundary value $T_c^{N_s}$. The shell-side fluid enters the MSTHE in a superheated vapor state. The heat transfer model for the superheated region (Eqs. (8) - (12)) is solved progressively until the fluid near the cooling tube wall reaches the saturation point, or until $k = N_s$ if saturation is not reached.

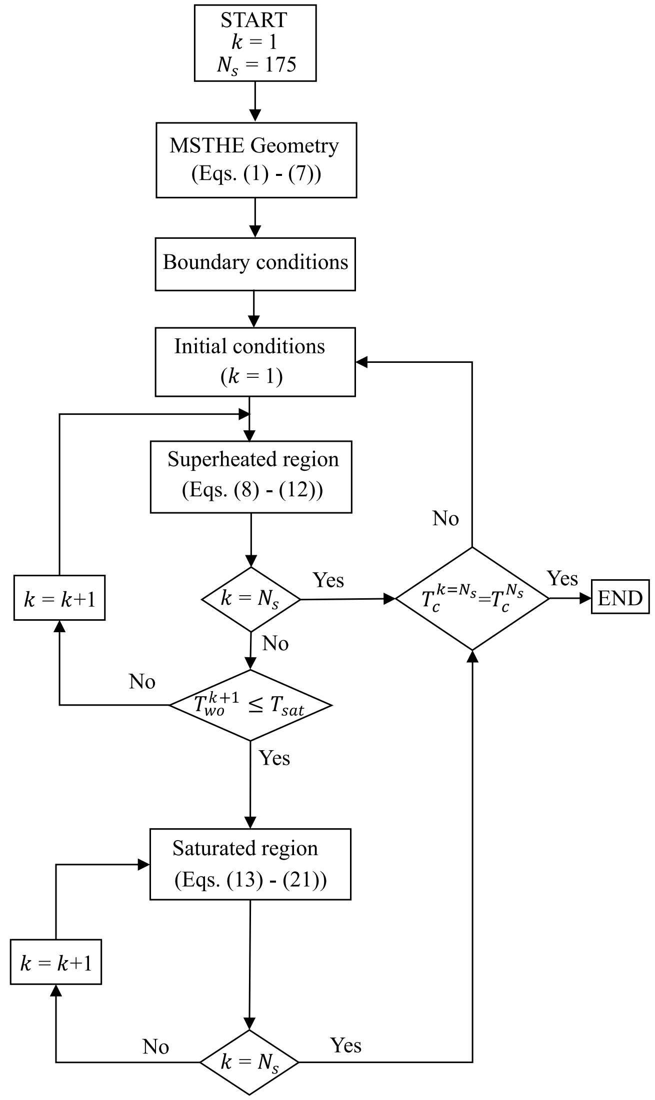

Fig. 4. Flow diagram of the numerical procedure for solving the thermal-hydraulic model of the MSTHE.

Once the shell fluid in the near-wall region reaches the dew point, the condensation model for the saturated region (Eqs. (13) - (21)) is applied to the remaining sections. Equations are iteratively solved until the last section $k = N_s$ is reached. Finally, it is verified whether the calculated tube-side inlet temperature $T_c^{k=N_s}$ agrees with the specified boundary condition $T_c^{N_s}$ within a tolerance of 0.1 °C. If the condition is met, the computation ends. If not, a new guess for $T_c^{k,*}$ is generated using a relaxation-based Newton-Raphson correction, and the entire model is recalculated until convergence is achieved.

2.5. ***Number of sections, N_s***

The number of sections N_s into which the heat exchanger was discretized was determined by balancing computational accuracy and efficiency. Increasing N_s reduces the spatial discretization step, thereby improving the resolution of the varying thermophysical properties of the scCO$_2$ and the local condensation process along the MSTHE. However, a higher number of sections also leads to a considerable increase in computational time, since the full calculation procedure shown in Fig. 4 must be executed for each division. To determine the optimal value of N_s, the MSTHE model was run under the nominal boundary conditions (100 % cycle load) shown in Table 1, with N_s varying from 50 to 1000. It was assumed that an optimal N_s would be the minimum value for which the relative error in key output variables (T_c^{out}, T_h^{out}, Δp_c, Δp_h and $\dot{N}_f$) did not exceed 0.1 %, compared to the results obtained with $N_s = 1000$.

Fig. 5 shows the variation of these output variables with respect to N_s on a logarithmic scale. As expected, the relative errors decrease with increasing N_s. However, for T_c^{out}, T_h^{out} and $\dot{N}_f^{out}$, minor fluctuations are observed. These fluctuations are attributed to the local uncertainties in the calculation of T_f within each section, which propagate along the

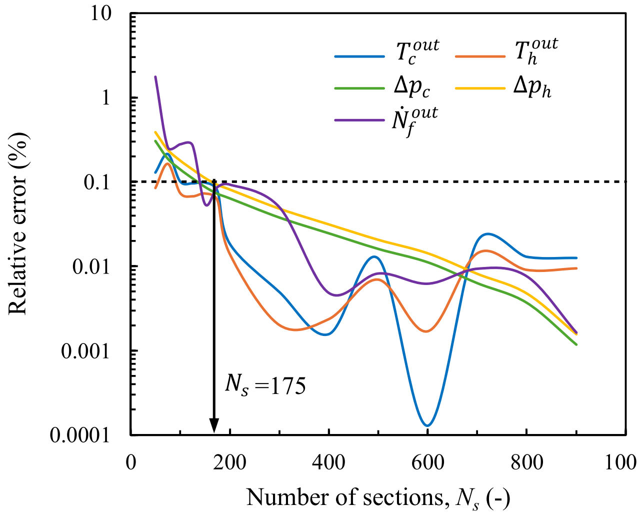

Fig. 5. Evolution of the output variables T_c^{out}, T_h^{out}, Δp_c, Δp_h and $\dot{N}_f^{out}$ as a function of the number of sections N_s. For $N_s = 175$, the relative errors are below 0.1 %.

length of the MSTHE and slightly affect the final output value. Based on the analysis shown in Fig. 5, it was determined that for $N_s = 175$, the relative error in all evaluated output variables remains below 0.1 %. Therefore, the value of $N_s = 175$ was selected.

3. Results and discussion

Section 3.1 presents the baseline geometrical configuration of the MSTHE, validated in Section 3.2. This geometrical configuration serves as the reference for the thermal-hydraulic performance assessments conducted in Sections 3.3 and 3.4, as a function of the geometrical variables and the cycle load level, respectively.

3.1. Baseline geometrical configuration

First, a baseline geometrical configuration of the MSTHE was established to comply with the nominal operating conditions given in Table 1 (at 100 % of cycle load). To this end, the design constraints for MSTHEs given in Table 4, proposed by Jiang et al. [34], were considered. Based on these constraints, a heat exchanger configuration consisting of 65,000 tubes with an outer diameter of 1.8 mm, arranged in a triangular pattern with a pitch of $1.25D_{to}$, was adopted. The exchanger length was determined through trial-and-error to achieve a thermal power of 10 $\mathrm{MW_{th}}$ under nominal conditions, resulting in a length of 3500 mm. The resulting baseline MSTHE configuration is shown in Table 5.

Fig. 6 depicts the temperature profiles along the axial direction of the MSTHE, obtained under nominal conditions according to the exchanger configuration in Table 5. It can be seen that the pinch-point of 4.7 °C occurs at the dew point temperature of the hot gases, 118.6 °C. The temperatures of the condensate film and the inner and outer walls of the tube are close to each other. This is due to the low resistance to heat transfer by convection in the condensate film and conduction through the tube wall.

3.2. Model validation

The reliability of the results produced by the MSTHE model was assessed through a validation process. In the absence of experimental data, the primary output variables of the model were compared with the results obtained from overall mass and energy balances calculated using Aspen Plus [31]. Fig. 7 shows the flow diagram implemented in Aspen Plus. The cold inlet stream (MCI) is heated in a heat exchanger (H) by thermal energy transferred from the hot stream (MHI), which is cooled in a separate heat exchanger (C). The temperatures, pressures, and mass flow rates of the hot (MHI) and cold (MCI) streams entering the system were set according to the nominal operating conditions (100 % cycle load) shown in Table 1. Additionally, the outlet temperature of the cold stream (MCO) was fixed at 138 °C, as defined in Table 1. This approach allows for a direct comparison between the output values obtained from the numerical integration of the MSTHE model and the resulting mass and energy balances resolved in Aspen Plus.

Table 6 presents the comparison between the main output parameters obtained with the MSTHE model and those from Aspen Plus. The largest deviations were found in the prediction of the molar fraction of H_2O and CO_2, 4.44 % and 6.51 %. The low relative errors reported in Table 6 confirm that the MSTHE model is capable of reliably capturing the condensation and heat transfer phenomena under the evaluated conditions.

Table 4
Design constraints of a MSTHE [34].

Parameter	Unit	Lower limit	Upper limit
Number of tubes, N_t	-	47,000	80,000
Outer shell diameter, D_{so}	mm	-	2300
Tube length, L	mm	-	8000
Pitch, P_t/D_{to}	-	1.25	1.5
Outer tube diameter, D_{to}	mm	1.0	3.5

Table 5
Baseline geometry configuration of the MSTHE.

Parameter	Unit	Value
Number of tubes, N_t	-	65,000
Outer shell diameter, D_{so}	mm	600
Tube length, L	mm	3500
Pitch, P_t/D_{to}	-	1.25
Outer tube diameter, D_{to}	mm	1.8
Tube arrangement	-	triangle

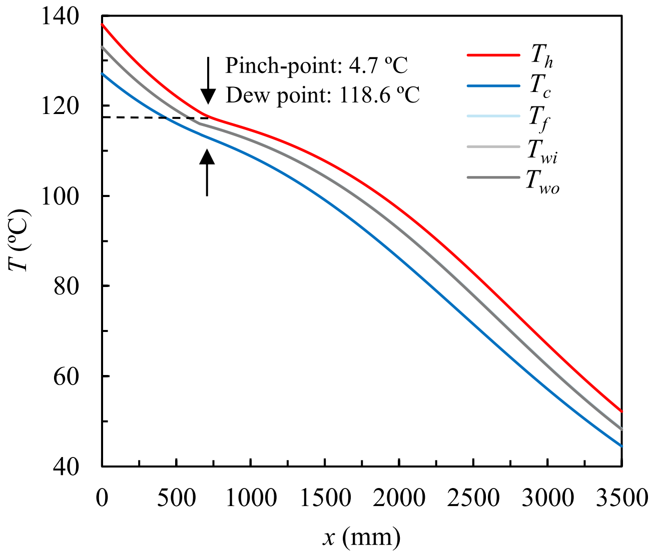

Fig. 6. Temperature profiles along the heat exchanger x-direction. under nominal conditions, the pinch-point of 4.7 °C occurs at the dew point of the hot gases, 118.6 °C.

In Section 3.3, a sensitivity study is conducted on the MSTHE performance as a function of the geometric design variables.

3.3. Sensitivity study of geometrical variables

This section evaluates how the major geometric parameters of the MSTHE influence its thermal-hydraulic performance. The analysis was based on the baseline MSTHE design presented in Table 5; with the boundary conditions fixed at the nominal values (100 % of cycle load) listed in Table 1. Fig. 8 shows the performance maps of the MSTHE as a function of N_t and D_{to}, for two pitch values: $P_t = 1.25D_{to}$ and $P_t = 1.45D_{to}$ The performance maps include the thermal power (a and b), overall heat transfer coefficient (c and d), effectiveness (e and f), and pressure drops on the cold-side (g and h), and hot-side (i and j). The effectiveness, defined in Eq. (39), represents the ratio between the actual heat flow exchanged and the theoretical maximum. The N_t ranges from 50,000 to 80,000, and D_{to} from 1.5 mm to 3 mm; values commonly reported in the MSTHE literature [24,34].

$$\varepsilon = \frac{\dot{Q}}{\left(\dot{m}\bar{c}_p\right)_{min}\left(T_h^{in} - T_c^{in}\right)} \qquad (39)$$

3.3.1. *Effect of the number of tubes, N_t*

Fig. 8(a) shows that increasing N_t causes a reduction of the thermal power exchanged in the MSTHE, for a constant P_t and D_{to}. For a P_t value of $1.25D_{to}$, the thermal power drops from 10 $\mathrm{MW_{th}}$ for 50,000 tubes to about 8.3 $\mathrm{MW_{th}}$ for 80,000 tubes. This thermal power drop is caused by

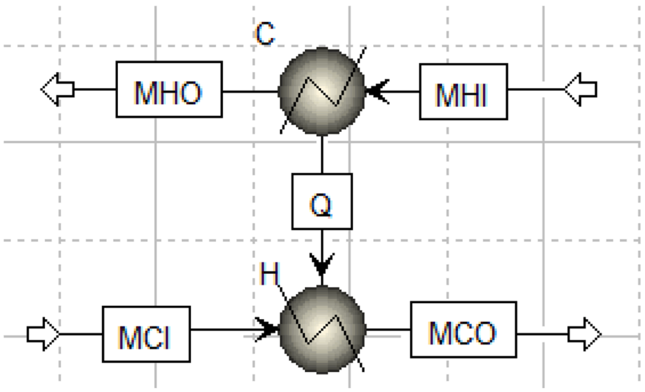

Fig. 7. Flow diagram of the model implemented in Aspen Plus to perform the MSTHE model validation.

the reduction of the flow velocities on both the shell and tube sides, which diminish the heat transfer rates and the operating effectiveness, as illustrated in Figs. 8(c) and 8(e). The reduction in the tube-side velocity is directly related to the increase of the cross-sectional flow area. It was also found that the shell-side flow passage area scales proportionally with the number of tubes, as shown in Eq. (40).

$$A_{ph} = \frac{\pi N_t}{4}\left[\frac{4P_t^2(CL)}{\pi(CTP)} - D_{to}^2\right] \tag{40}$$

Lower flow velocities throughout the exchanger also lead to a decrease in pressure drops, as shown in Figs. 8(g) and 8(i). When P_t is fixed at $1.25D_{to}$, the tube-side pressure drop ranges from 4 bar to 8 bar for 50,000 tubes depending on tube diameter, but falls below 1 bar when the number of tubes exceeds 60,000, regardless of the P_t value. This finding suggests that, under the studied boundary conditions, an MSTHE bundle should contain >60,000 tubes to maintain the tube-side pressure drop under 1 bar. This condition is favorable for an efficient operation of the NET Power cycle.

3.3.2. *Effect of the tube diameter, D_{to}*

For a fixed P_t and N_t, increasing D_{to} results in a slight increase in both the thermal power and effectiveness, as shown in Figs. 8(a) and 8(e). This increase is due to a larger heat exchange area, which exceeds the decrease of the heat transfer coefficient, resulting in a net increase of the thermal conductance. Consequently, the thermal power and effectiveness reach maximum values of 10 $\mathrm{MW_{th}}$ and 90 %, respectively, for 50,000 microtubes with an outer diameter of 3 mm. However, the resulting MSTHE configuration would lack compactness and require a substantial amount of material, leading to higher costs and a slower dynamic response to changes in the operating point. The heat transfer coefficient reaches a maximum value of about 1.6 kW $\mathrm{m^{-2}\ K^{-1}}$ for 50,000 tubes with a 1.5 mm outer diameter, as a consequence of the high Reynolds numbers. Nevertheless, as plotted in Figs. 8(g) and 8(i), the corresponding pressure drops are excessively high, and would compromise the efficient operation of the NET Power cycle.

Table 6
Comparison of the main output parameters of the MSTHE model and the global mass and energy balances in Aspen Plus. all relative errors are below 6.51 %, indicating that the heat and mass transfer mechanisms of the MSTHE model are reliable.

Output parameter	MSTHE model	Aspen Plus Mass & energy balances	RE* (%)
Cold fluid temperature, T_c^{out} (°C)	137.10	138	0.65
Hot fluid temperature, T_h^{out} (°C)	52.16	52.09	0.13
Heat flow, $\dot{Q}$ ($\mathrm{MW_{th}}$)	9.89	10.00	1.11
Condensate molar flow, $\dot{N}_f^{out}$ ($\mathrm{mol\ s^{-1}}$)	74.50	74.36	0.19
H_2O mole fraction, $\hat{y}_{H_2O,h}^{out}$ (%)	0.45	0.48	4.44
CO_2 mole fraction, $\hat{x}_{CO_2,f}^{out}$ (%)	1.33	1.24	6.51

[*] RE: Relative Error.

3.3.3. *Effect of the pitch, P_t*

Increasing P_t, while keeping N_t and D_{to} constant, leads to an increase of the shell diameter and shell flow passage area. This diminishes the shell flow velocity and, consequently, reduces the thermal power, heat transfer coefficient, effectiveness, and pressure drop on the shell-side, as depicted in Figs. 8(b), 8(d), 8(f) and 8(j), respectively. In particular, increasing P_t from $1.25D_{to}$ to $1.45D_{to}$ results in the following changes: the maximum thermal power drops from 10.04 $\mathrm{MW_{th}}$ to 9.70 $\mathrm{MW_{th}}$; the heat transfer coefficient decreases from 1.64 kW $\mathrm{m^{-2}\ K^{-1}}$ to 1.15 kW $\mathrm{m^{-2}\ K^{-1}}$; the effectiveness falls from 90.35 % to 87.00 %; and the shell-side pressure drop reduces from 4.38 bar to 0.74 bar. Since the tube-side flow velocity remains constant regardless of P_t, the pressure drop on the tube-side is unaffected by changes in the P_t value.

Once the influence of geometric variables on the MSTHE performance has been assessed, Section 3.4 investigates the behavior of the MSTHE under cycle-relevant part-load conditions.

3.4. *Part-load behavior of the micro shell-and-tube heat exchanger*

To assess the performance of the MSTHE under partial cycle load conditions, the MSTHE model was evaluated using the off-design boundary conditions presented in Table 1, which were obtained from an off-design thermodynamic model of the NET Power cycle. All variables, except the shell fluid pressure, decrease as the cycle load is reduced. Fig. 9 illustrates the variation of (a) the thermal power and effectiveness of the MSTHE, and (b) the overall heat transfer coefficient and pressure drops, as a function of the cycle load degree (based on the cycle fuel input).

The thermal power transferred in the heat exchanger decreases with the reduction of the cycle load degree, as can be seen in Fig. 9(a). This is due to the decrease in the mass flow rates on both the shell and tube sides. The effectiveness of the heat exchanger follows a parabolic decrease from 89.22 %, under nominal conditions, to 65.13 % at 20 % of cycle load. Despite the decrease of the inlet temperatures of both the hot and cold fluids with decreasing cycle load (as listed in Table 1), the maximum temperature difference in the exchanger, $T_{h,in}$ - $T_{c,in}$, remains approximately constant. Consequently, according to the effectiveness definition in Eq. (39), the combination of this effect with the lower thermal power results in the observed drop of the effectiveness.

A lower thermal power also leads to a reduction in the flow velocities on both sides of the exchanger, reducing the heat transfer by turbulent action. As a result, both the heat transfer coefficient and the pressure drops diminish, as can be seen in Fig. 9(b). The pressure drop on the tube-side drops more steeply than on the shell-side as the cycle load decreases. Furthermore, the heat transfer coefficient shows a moderate decline from nominal conditions down to a 50 % of cycle load. Below 50 %, it drops rapidly to 30 %, and then remains nearly constant between 30 % and 20 % of cycle load. This behavior can be attributed to the evolution of the hot- and cold-side heat transfer coefficients, α_h and α_c, as a function of the cycle load. These trends are shown in Figs. 10(a) and 10(b).

The coefficients α_h and α_c decrease smoothly as the cycle load decreases from 100 % to approximately 50 %. This trend is attributed to the moderate reduction in the mass flow rates with the cycle load through the MSTHE, as indicated in Table 1. Below a cycle load of 40 %, the pressure reduction in the tube-side fluid leads to a significant reduction in α_c, due to the presence of a low-density, gas-like supercritical phase.

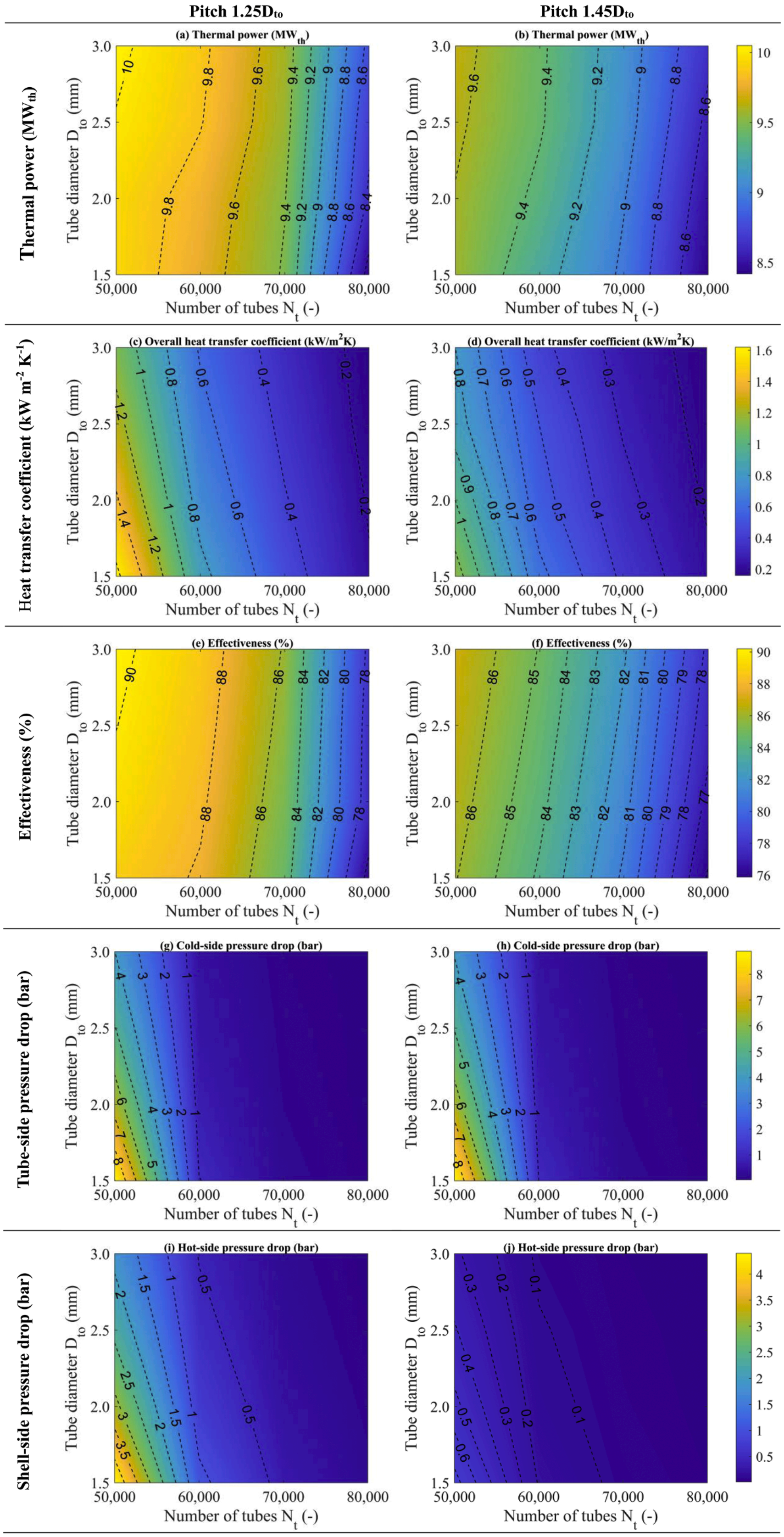

Fig. 8. Performance maps of the MSTHE as a function of the number of tubes N_t and tube diameter D_{to}, for two pitch values: $P_t = 1.25D_{to}$ and $P_t = 1.45D_{to}$.

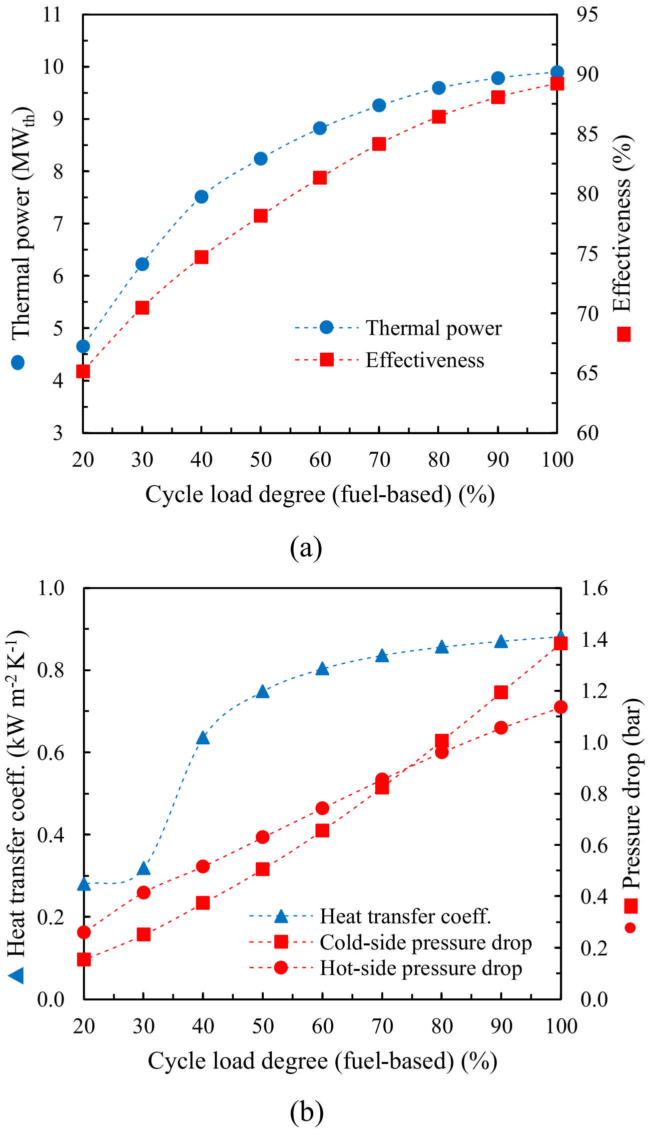

Fig. 9. Performance indexes of the MSTHE as a function of the cycle load degree (based on the fuel input). (a) Thermal power and effectiveness, and (b) overall heat transfer coefficient and pressure drops. These thermodynamic indexes decrease as the cycle load decreases.

As the load level is further reduced to 30 % and 20 %, the tube-side scCO$_2$ approaches its critical pressure. As shown in Fig. 11, this condition leads to an abrupt increase in the local specific heat capacity within the pseudo-critical region, where the supercritical phase transition between gas-like and liquid-like properties occurs. Thus, the Prandtl number increases significantly by virtue of the heat capacity. This results in the substantial local increase of α_c, observed in Fig. 10(b), at a distance between 2500 mm and 3500 mm along the tube length. In addition, the reduction of the thermal power and inlet fluid temperature at low cycle loads promote the amplification of the peak values of α_c [51]. Consequently, the sudden rise in α_c at a 20 % of cycle load causes the overall heat transfer coefficient to remain nearly constant between 20 % and 30 % of cycle load. This finding suggests that operating conditions near the critical pressure of the tube-side scCO$_2$ enhance the heat transfer effectiveness of the MSTHE at minimum NET Power cycle load degrees.

The sharp variation of α_c near the pseudo-critical temperature of the scCO$_2$ at low cycle loads leads to a decrease in the condensate film temperature. This, in turn, results in: (i) an increase in the sensible heat transferred from the shell-side hot gas to the condensate phase, and (ii) a higher condensate formation rate. These effects cause a localized surge in the heat flux from the shell-side to the tube-side in the region of the MSTHE where the tube-side scCO$_2$ approaches its pseudo-critical temperature. Consequently, the axial temperature gradients of both the hot and cold fluids (dT_h/dx and dT_c/dx) become markedly steep at this location. This behavior can be seen in Fig. 12, which shows the evolution of (a) dT_h/dx and (b) dT_c/dx along the MSTHE, as a function of the cycle load degree.

Such abrupt temperature gradients can compromise the structural integrity of the microtubes by inducing thermal shock phenomena, which may promote material cracking and differential thermal expansion. Under cyclic part-load operation, the repeated expansion and contraction of the microtube bundle can lead to the accumulation of thermo-mechanical fatigue damage, potentially reducing the service life of the MSTHE and imposing more stringent inspection and maintenance requirements. In addition, corrosion mechanisms on the heat exchanger surfaces may be accelerated [21]. Moreover, the inherently non-uniform heat flux distribution along the tube wall, combined with circumferential wall temperature gradients induced by buoyancy-driven effects, further amplifies the development of thermal stresses in the microtubes [65,66]. From an operation perspective, these findings highlight the importance of carefully managing part-load transient and load variation rates in order to mitigate excessive thermal gradients. From a mechanical design standpoint, the results also reveal an additional advantage of MSTHEs over PCHEs: the floating microtube bundle configuration provides enhanced tolerance to thermal expansion and stress accommodation, whereas the rigid PCHE structure is more susceptible to stress accumulation and potential structural damage under similar operating conditions.

It was found that the proximity of the scCO$_2$-side to its critical point at low cycle loads has significant implications for the filmwise condensation process occurring on the outer microtube walls. Fig. 13 depicts the evolution of (a) $\dot{n}$, (b) $\widehat{y}_{H_2O,h} - \widehat{y}_{H_2O,f}$, and (c) δ along the MSTHE, as a function of the cycle load degree.

It can be found in Fig. 13(a) that the shell-side wet gases reach the saturation point progressively closer to the hot-end of the MSTHE as the cycle load degree decreases. The overall trend of $\dot{n}$ along the MSTHE results similar for all cycle load degrees; $\dot{n}$ initially increases, reaches a peak value, and then gradually declines due to the reduction in the vapor partial pressure in the shell-side fluid flow. However, for cycle load degrees of 40 %, 30 % and 20 %, $\dot{n}$ exhibits a second peak at axial positions of about 1500 mm, 2000 mm and 2750 mm, respectively. This second peak of $\dot{n}$ increases the local amount of condensation heat released in those regions of the MSTHE, which enhances the overall heat transfer rates at low cycle loads.

When observing Figs. 13(a) and 10(b), it can be deduced that the peaks of $\dot{n}$ occur when the tube-side scCO$_2$ reaches the pseudo-critical temperature. The sudden increase of α_c within the pseudo-critical region causes a sharp reduction of the condensate film temperature, as previously stated. This temperature drop leads to a higher difference of the H$_2$O mole fraction between the hot gas bulk and the film interface, $\widehat{y}_{H_2O,h} - \widehat{y}_{H_2O,f}$, as illustrated in Fig. 13(b). Consequently, the vapor transport rate from the gas bulk to the vapor-liquid interface is locally intensified, with a consequent improvement of the heat transfer performance. Conversely, the second peak of $\dot{n}$ leads to a rapid increase in the condensate molar flow rate $\dot{N}_f$, resulting in a sudden thickening of the condensate film, as shown in Fig. 13(c). Accordingly, the thermal resistance of the film slightly increases in the region near the pseudo-critical temperature of the tube-side scCO$_2$ at low cycle load conditions.

In general, as can be found in Fig. 13(c), the condensate film thickens as the cycle load decreases. This behavior is attributed to the reduction in mass flow rates through the heat exchanger, which leads to a lower shell-side flow velocity. As a result, the velocity gradient near the vapor-liquid interface diminishes, thereby reducing the interfacial shear stress τ_{hf}. The reduction of τ_{hf}, under partial loads, also causes a mitigation of

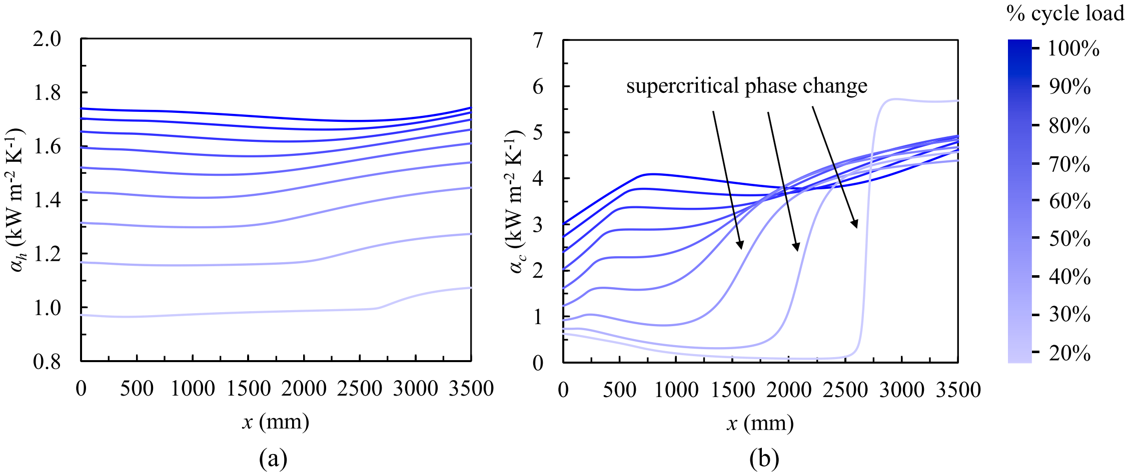

Fig. 10. Evolution of the convective heat transfer coefficient on (a) the shell-side α_h and (b) the tube-side α_c along the heat exchanger x-direction, as a function of the cycle load degree (fuel-based). In the supercritical phase change, α_c changes rapidly due to the variation in the Prandtl number of the fluid near the pseudo-critical temperature.

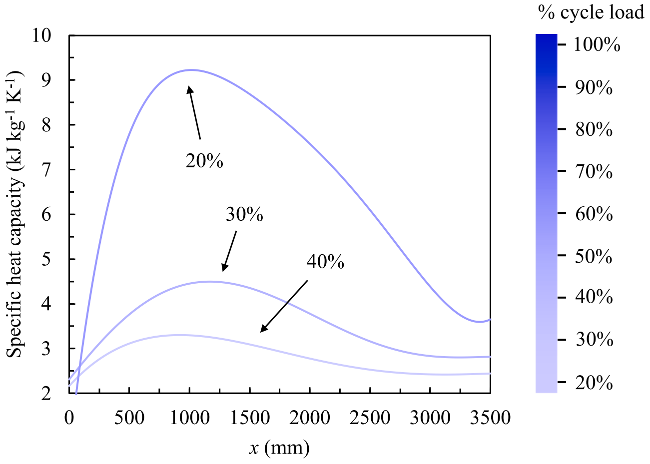

Fig. 11. Evolution of specific heat capacity along the MSTHE length for cycle load levels of 40 %, 30 %, and 20 %. The local peaks reflect the pseudo-critical phase change of the tube-side CO$_2$ in supercritical regime. This results in the increases of the heat transfer coefficients, α_c, illustrated in Fig. 10.

turbulent fluctuations within the condensate film. As a result, both heat and mass transfer rates within the condensate are reduced. This reduction of the transport rates within the condensate promotes the accumulation of CO$_2$ molecules at the film interface, further increasing the resistance to vapor transfer in the wet gas phase.

Fig. 14 represents the evolution of the pinch-point as a function of the cycle load degree. At nominal conditions, the pinch-point presents a value of 4.7 °C and is located 700 mm from the hot-end of the heat exchanger. This location coincides with the saturation temperature of the shell-side hot gas, as discussed in Section 3.1. As the cycle load is reduced from 100 % to 90 %, the pinch-point shifts towards the cold-end of the exchanger and rises slightly to 5.6 °C. Thereafter, as the cycle load degree decreases further from 90 % to 20 %, the pinch-point gradually declines while remaining at the cold-end of the MSTHE.

4. Conclusions

This paper presents as a novelty a comprehensive investigation of the thermal-hydraulic performance of a micro shell-and-tube heat exchanger (MSTHE) operating under partial load conditions, for its application in the innovative oxy-combustion-based NET Power cycle. The study focuses on the condensative low-temperature section of the thermal recuperator, which operates in the vicinity of the critical point

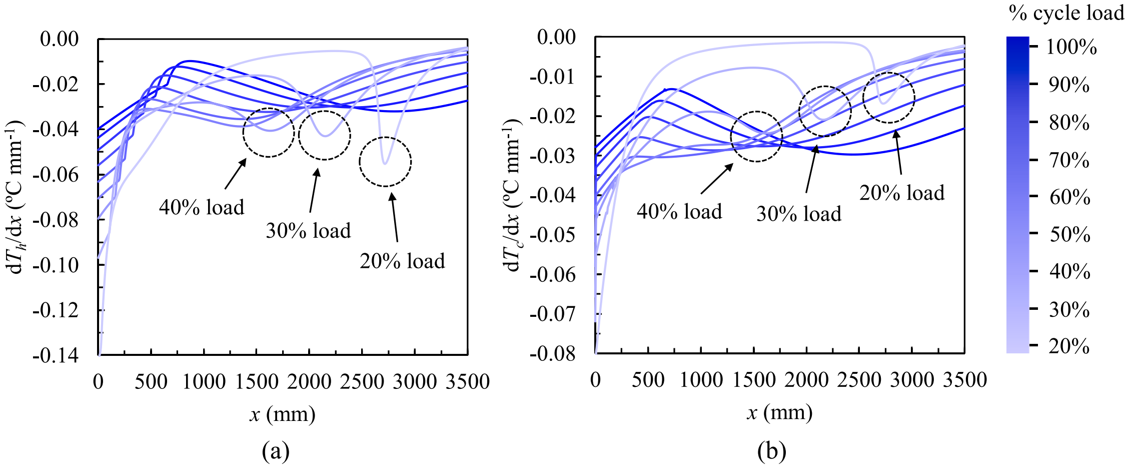

Fig. 12. Axial temperature gradients on (a) the shell-side dT_h/dx and (b) the tube-side dT_c/dx along the heat exchanger x-direction, as a function of the cycle part load degree (fuel-based). The strong axial temperature gradients, caused by the supercritical phase change, may compromise the mechanical integrity of the MSTHE.

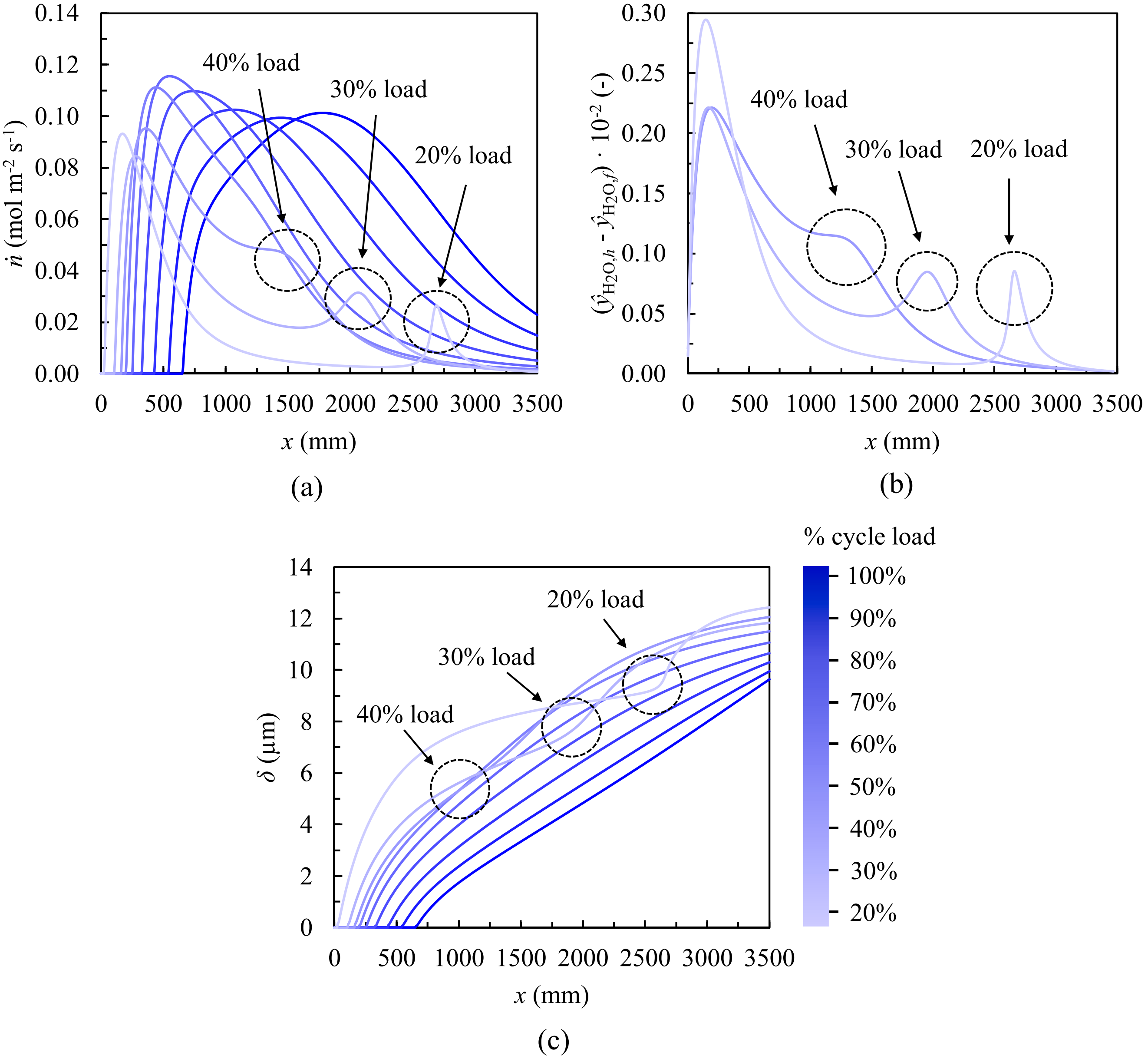

Fig. 13. (a) condensing molar flux $\dot{n}$, (b) H_2O molar fraction gradient $\hat{y}_{H_2O,h} - \hat{y}_{H_2O,f}$ and (c) condensate film thickness δ, along the heat exchanger x-direction, as a function of the cycle load degree (fuel-based). The rapid increase in α_c during the supercritical phase change instantaneously lowers the condensate temperature, leading to secondary peaks in $\dot{n}$ and $\hat{y}_{H_2O,h} - \hat{y}_{H_2O,f}$. The condensate film thickens as the cycle load decreases.

of CO_2. The objective is to promote, for the first time, a feasible technological transition from printed circuit heat exchangers (PCHE) to MSTHE, which, according to literature, offer numerous techno-economic advantages.

To this end, a novel thermal-hydraulic model of a horizontally-oriented MSTHEs was developed, capable of capturing the non-linear pressure and temperature dependence of supercritical CO_2 (sCO_2) properties, as well as representing partial filmwise condensation of the turbine exhaust gases. Subsequently, the performance of the MSTHE was assessed as a function of its geometrical design parameters and the NET Power cycle load level. The key findings of this research are the following:

- Reducing the number of tubes improves the performance of the MSTHE. However, to ensure a proper operation of the NET Power cycle, under the boundary conditions considered in this study, the MSTHE must contain at least 60,000 tubes, which allows maintaining the tube-side pressure drop below 1 bar. Increasing the tube diameter from 1.5 to 3.0 mm results in a slight increase in thermal power and effectiveness. Nevertheless, this penalizes the compactness and increases the dynamic response time. The effect of the microtube diameter on bending was not assessed, representing a limitation of the study. It was found that increasing the tube pitch reduces the thermal effectiveness, although it decreases the pressure drop on the shell-side.
- At nominal conditions, the MSTHE effectiveness is high, 89.2 %, and progressively decreases to 65.1 % when the cycle load is reduced to 20 %, with a thermal power drop from 10 to 4.6 MW_{th}. The overall heat transfer coefficient decreases smoothly between 100 % and 40 % cycle load, falls rapidly from 40 % to 30 %, and remains approximately constant between 30 % and 20 %.
- Numerical results revealed that the favorable maintenance of the heat transfer coefficient between 30 % and 20 % load is due to the pseudo-critical phase property transition on the sCO_2-side, which

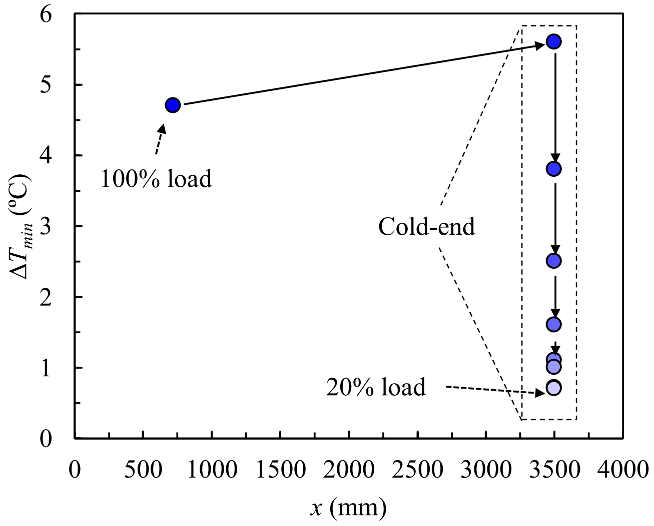

Fig. 14. Evolution of the pinch point, ΔT_{min}, as a function of the cycle load degree (fuel-based). under nominal conditions, the pinch point is 4.7 °C and is located at the saturation point of the shell-side gases. As the cycle load decreases, the pinch point lowers and shifts toward the cold-end of the MSTHE.

abruptly increases its local heat transfer coefficient. This, in turn, causes a sudden reduction of the condensate film temperature, which locally intensifies the condensation heat release rates. However, it was found that this originates strong axial temperature gradients within the microtubes, which could compromise their structural integrity. While the floating microtube bundle of MSTHEs can accommodate the thermal stresses, the rigid compact block structure of PCHEs may suffer damage. This novel finding reveals an additional key advantage of MSTHEs over PCHEs, which contributes to improving the thermal effectiveness and mechanical performance of future heat recuperation units for the NET Power cycle.

- The MSTHE proposed in this work features a compact design that facilities its construction and reduces thermal inertia, a pivotal advantage given the high thermal demand. As a trade-off, the system is exposed to thermal gradients that may induce mechanical fatigue stresses through repeated expansion and contraction of the microtube bundle.

Future research could focus on the following key aspects:

- Conducting a MW-scale experimental validation of the model developed in this work under operating conditions representative of the NET Power cycle.
- Performing a comprehensive experimental comparison of the thermal-hydraulic performance of PCHE and MSTHE heat exchange architectures under part-load conditions of the NET Power cycle. This analysis would enable the derivation of relevant conclusions and guide future design strategies for the thermal recuperation unit.
- Extending the model developed in this work to cover the remaining sections of the recuperator, which represents a limitation of this study, with the aim of designing an optimal heat exchange network based on MSTHE units.
- From a mechanical design perspective, investigating the vertical orientation of a MSTHE to mitigate mechanical stresses in the tubes induced buoyancy and thermal stratification effects.

CRediT authorship contribution statement

Iván Velázquez: Writing – original draft, Software, Resources, Methodology, Investigation, Formal analysis, Data curation, Conceptualization. **Frederiek Demeyer:** Writing – review & editing, Visualization, Resources, Project administration, Conceptualization. **Miriam Reyes:** Writing – review & editing, Supervision, Project administration, Funding acquisition, Conceptualization.

Declaration of competing interest

The authors declare that they have no known competing financial interests or personal relationships that could have appeared to influence the work reported in this paper.

Acknowledgements

The research work was funded by the University of Valladolid, Spain, through the research project 061/2209311. Authors would like to acknowledge the entities Engie and TES-H2, and the research group in thermal engines and renewable energies (MyER), from the University of Valladolid, for the technical contribution during the realization of this work.

Supplementary materials

Supplementary material associated with this article can be found, in the online version, at doi:10.1016/j.ijheatmasstransfer.2026.128419.

Data availability

Data will be made available on request.

References

[1] Energy institute, Statistical review of world energy. 73rd edition, 2024.
[2] IPCC, 2023: Climate change 2023: synthesis report. contribution of working groups I, II and III to the sixth assessment report of the intergovernmental panel on climate change [Core Writing Team, H. Lee and J. Romero (eds.)]. IPCC, Geneva, Switzerland., 2023. https://doi.org/10.59327/IPCC/AR6-9789291691647.
[3] S. Aryal, S. Lee, K. Jeong, Investigating the effects of design parameters on heat transfer rate and fouling in full-scale gas-to-gas coolers: a numerical study, Int. J. Therm. Sci. 211 (2025) 109721, https://doi.org/10.1016/j.ijthermalsci.2025.109721.
[4] D.Y.C. Leung, G. Caramanna, M.M. Maroto-Valer, An overview of current status of carbon dioxide capture and storage technologies, Renew. Sustain. Energy Rev. 39 (2014) 426–443, https://doi.org/10.1016/j.rser.2014.07.093.
[5] T. Kuramochi, A. Ramírez, W. Turkenburg, A. Faaij, Comparative assessment of CO_2 capture technologies for carbon-intensive industrial processes, Prog. Energy Combust. Sci. 38 (2012) 87–112, https://doi.org/10.1016/j.pecs.2011.05.001.
[6] M.A. Nemitallah, M.A. Habib, H.M. Badr, S.A. Said, A. Jamal, R. Ben-Mansour, E. M.A. Mokheimer, K. Mezghani, Oxy-fuel combustion technology: current status, applications, and trends, Int. J. Energy Res. 41 (2017) 1670–1708, https://doi.org/10.1002/er.3722.
[7] F. Climent Barba, G. Martínez-Denegri Sánchez, B. Soler Seguí, H. Gohari Darabkhani, E.J. Anthony, A technical evaluation, performance analysis and risk assessment of multiple novel oxy-turbine power cycles with complete CO_2 capture, J. Clean. Prod. 133 (2016) 971–985, https://doi.org/10.1016/j.jclepro.2016.05.189.
[8] L. Mancuso, N. Ferrar, P. Chiesa, E. Martelli, M. Romano, oxy-combustion turbine power plants, 2015. www.ieaghg.org. (accessed March 9, 2023).
[9] W. Chan, T. Morosuk, X. Li, H. Li, Allam cycle: review of research and development, Energy Convers. Manag. 294 (2023) 117607, https://doi.org/10.1016/j.enconman.2023.117607.
[10] I. Velázquez, F. Demeyer, M. Reyes, Investigation of the impact of the thermodynamic property method on the performance, preliminary component sizing and maximum efficiency configuration of the NET power cycle, Appl. Therm. Eng. (2025) 126491, https://doi.org/10.1016/j.applthermaleng.2025.126491.
[11] A. Rogalev, E. Grigoriev, V. Kindra, N. Rogalev, Thermodynamic optimization and equipment development for a high efficient fossil fuel power plant with zero emissions, J. Clean. Prod. (2019) 236, https://doi.org/10.1016/j.jclepro.2019.07.067.
[12] R. Scaccabarozzi, M. Gatti, E. Martelli, Thermodynamic analysis and numerical optimization of the NET power oxy-combustion cycle, Appl. Energy 178 (2016) 505–526, https://doi.org/10.1016/j.apenergy.2016.06.060.
[13] K. Brun, P. Friedman, R. Dennis, Fundamentals and Applications of Supercritical Carbon Dioxide (sCO_2) Based Power Cycles, Woodhead Publishing Series in Energy, 2017.
[14] R.J. Allam, B.A. Forrest, J.E. Fetvedt, Method and system for power production with improved efficiency, U.S. Pat. Appl. (2018), 2018007343415 Mar.
[15] C. Mitchell, V. Avagyan, H. Chalmers, M. Lucquiaud, An initial assessment of the value of Allam Cycle power plants with liquid oxygen storage in future GB

electricity system, Int. J. Greenh. Gas Control 87 (2019) 1–18, https://doi.org/10.1016/j.ijggc.2019.04.020.

[16] A. Meshram, A.K. Jaiswal, S.D. Khivsara, J.D. Ortega, C. Ho, R. Bapat, P. Dutta, Modeling and analysis of a printed circuit heat exchanger for supercritical CO_2 power cycle applications, Appl. Therm. Eng. 109 (2016) 861–870, https://doi.org/10.1016/j.applthermaleng.2016.05.033.

[17] M. Marchionni, L. Chai, G. Bianchi, S.A. Tassou, Numerical modelling and transient analysis of a printed circuit heat exchanger used as recuperator for supercritical CO_2 heat to power conversion systems, Appl. Therm. Eng. 161 (2019) 114190, https://doi.org/10.1016/j.applthermaleng.2019.114190.

[18] R. Allam, S. Martin, B. Forrest, J. Fetvedt, X. Lu, D. Freed, G.W. Brown, T. Sasaki, M. Itoh, J. Manning, Demonstration of the Allam cycle: an update on the development status of a high efficiency supercritical carbon dioxide power process employing full carbon capture. Energy Procedia, Elsevier Ltd, 2017, pp. 5948–5966, https://doi.org/10.1016/j.egypro.2017.03.1731.

[19] J.S. Kwon, S. Son, J.Y. Heo, J.I. Lee, Compact heat exchangers for supercritical CO_2 power cycle application, Energy Convers. Manag. 209 (2020) 112666, https://doi.org/10.1016/j.enconman.2020.112666.

[20] Y. Jiang, E.A. Liese, S.E. Zitney, D. Bhattacharyya, Dynamic modeling of microtube recuperators in an indirect supercritical carbon dioxide recompression closed Brayton power cycle, in: The 6th International Supercritical CO_2 Power Cycles Symposium, 2018.

[21] Y.H. Fan, G.H. Tang, X.L. Li, D.L. Yang, General and unique issues at multiple scales for supercritical carbon dioxide power system: a review on recent advances, Energy Convers. Manag. 268 (2022) 115993, https://doi.org/10.1016/j.enconman.2022.115993.

[22] L. Teeter, B. Adam, T. Wood, J.D. Tucker, Comparison of the corrosion of materials in supercritical carbon dioxide, air, and argon environments, Corros. Sci. 192 (2021) 109752, https://doi.org/10.1016/j.corsci.2021.109752.

[23] V. Firouzdor, K. Sridharan, G. Cao, M. Anderson, T.R. Allen, Corrosion of a stainless steel and nickel-based alloys in high temperature supercritical carbon dioxide environment, Corros. Sci. 69 (2013) 281–291, https://doi.org/10.1016/j.corsci.2012.11.041.

[24] L. Chordia, M.A. Portnoff, E. Green, High temperature heat exchanger design and fabrication for systems with large pressure differentials, Pittsburgh, PA, and Morgantown, WV (United States), 2017. https://doi.org/10.2172/1349235.

[25] H. Cai, S. Liang, C. Guo, T. Wang, Y. Zhu, Y. Jiang, Numerical investigation on heat transfer of supercritical carbon dioxide in the microtube heat exchanger at low reynolds numbers, Int. J. Heat. Mass Transf. 151 (2020) 119448, https://doi.org/10.1016/j.ijheatmasstransfer.2020.119448.

[26] H. Cai, Y. Jiang, T. Wang, S. Liang, Y. Zhu, Experimental investigation on convective heat transfer and pressure drop of supercritical CO_2 and water in microtube heat exchangers, Int. J. Heat. Mass Transf. 163 (2020) 120443, https://doi.org/10.1016/j.ijheatmasstransfer.2020.120443.

[27] H. Cai, Y. Jiang, T. Wang, S. Liang, C. Guo, Y. Zhu, An optimization of microtube heat exchangers for supercritical CO_2 cooling based on numerical and theoretical analysis, Int. Commun. Heat Mass Transf. 127 (2021) 105532, https://doi.org/10.1016/j.icheatmasstransfer.2021.105532.

[28] K. Jin, A.B. Krishna, Z. Wong, P.S. Ayyaswamy, I. Catton, T.S. Fisher, Thermohydraulic experiments on a supercritical carbon dioxide–air microtube heat exchanger, Int. J. Heat. Mass Transf. 203 (2023) 123840, https://doi.org/10.1016/j.ijheatmasstransfer.2022.123840.

[29] A.B. Krishna, K. Jin, P.S. Ayyaswamy, I. Catton, T.S. Fisher, Technoeconomic optimization of superalloy supercritical CO_2 microtube shell-and-tube-heat exchangers, Appl. Therm. Eng. 220 (2023) 119578, https://doi.org/10.1016/j.applthermaleng.2022.119578.

[30] A.B. Krishna, K. Jin, P.S. Ayyaswamy, I. Catton, T.S. Fisher, Modeling of supercritical CO_2 shell-and-tube heat exchangers under extreme conditions: part II: heat exchanger model, J. Heat Transf. 144 (2022), https://doi.org/10.1115/1.4053511.

[31] Aspen Plus | Leading Process Simulation Software | AspenTech, (n.d.). https://www.aspentech.com/en/products/engineering/aspen-plus (accessed June 12, 2023).

[32] I. Velázquez, F. Demeyer, M. Reyes, Optimization and performance evaluation of equations of state for supercritical CO_2-rich mixtures for application in the NET power cycle, J. Supercrit. Fluids. (2025) 106693, https://doi.org/10.1016/j.supflu.2025.106693.

[33] R.K. Shah, D.P. Srkulic, Fundamentals of Heat Exchanger Design, John Wiley & Sons, Inc., 2003.

[34] Y. Jiang, E. Liese, S.E. Zitney, D. Bhattacharyya, Optimal design of microtube recuperators for an indirect supercritical carbon dioxide recompression closed Brayton cycle, Appl. Energy 216 (2018) 634–648, https://doi.org/10.1016/j.apenergy.2018.02.082.

[35] J.M. Coulson, J.F. Richardson, Chemical Engineering, 6th ed., Elsevier, 1993 https://doi.org/10.1016/C2009-0-11215-1.

[36] Tubular Exchanger Manufacturers Association (TEMA), Standards of the tubular exchanger manufacturers association, 11th ed., 2023.

[37] M. Carlson, T. Conboy, D. Fleming, J. Pasch, Scaling considerations for SCO_2 cycle heat exchangers. Volume 3B: Oil and Gas Applications; Organic Rankine Cycle Power Systems; Supercritical CO_2 Power Cycles; Wind Energy, ASME, 2014, https://doi.org/10.1115/GT2014-27233.

[38] ASME International, ASME boiler and pressure Vessel, an international code: section 2 materials, part D: properties., 2019.

[39] P. Rączka, K. Wójs, Methods of thermal calculations for a condensing waste-heat exchanger, Chem. Process. Eng. 35 (2014) 447–461, https://doi.org/10.2478/cpe-2014-0034.

[40] K. Jeong, M.J. Kessen, H. Bilirgen, E.K. Levy, Analytical modeling of water condensation in condensing heat exchanger, Int. J. Heat. Mass Transf. 53 (2010) 2361–2368, https://doi.org/10.1016/j.ijheatmasstransfer.2010.02.004.

[41] O. Kunz, W. Wagner, The GERG-2008 wide-range equation of state for natural gases and other mixtures: an expansion of GERG-2004, J. Chem. Eng. Data 57 (2012) 3032–3091, https://doi.org/10.1021/je300655b.

[42] M.F. Monteiro, M.H. Moura-Neto, C.G. Pereira, O. Chiavone-Filho, Description of phase equilibrium and volumetric properties for CO_2 + water and CO_2 + ethanol using the CPA equation of state, J. Supercrit. Fluids. 161 (2020), https://doi.org/10.1016/j.supflu.2020.104841.

[43] J.S. Gallagher, R. Crovetto, J.M.H.L. Sengers, The thermodynamic behavior of the CO_2-H_2O system from 400 to 1000 K, up to 100 MPa and 30% mole fraction of CO_2, J. Phys. Chem. Ref. Data 22 (1993) 431–513, https://doi.org/10.1063/1.555938.

[44] A.P. Colburn, O.A. Hougen, Design of cooler condensers for mixtures of vapors with non-condensing gases, Ind. Eng. Chem. 26 (1934) 1178–1182, https://doi.org/10.1021/ie50299a011.

[45] A.P. Colburn, T.N. Drew, The Condensation of Mixed Vapors, American Institute of Chemical Engineers, New York, 1937.

[46] G. Ackermann, Combined heat and mass transfer at high temperature and partial pressure differences, Porsch. Ing. Wes. (1937).

[47] L. Cheng, G. Ribatski, J.R. Thome, Analysis of supercritical CO_2 cooling in macro- and micro-channels, Int. J. Refrig. 31 (2008) 1301–1316, https://doi.org/10.1016/j.ijrefrig.2008.01.010.

[48] H. Martin, Lecture On Heat Transfer II, Universitaet Karlsruhe (TH, 1990.

[49] V. Gnielinski, New equations for heat and mass transfer in the turbulent flow in pipes and channels, NASA STI/recon technical report a. 41 (1975) 8–16.

[50] X. Huai, S. Koyama, Heat transfer characteristics of supercritical CO_2 flow in small-channeled structures, Exp. Heat Transf. 20 (2007) 19–33, https://doi.org/10.1080/08916150600977424.

[51] I. Velázquez, D.A. Cantero, F. Demeyer, M. Reyes, Experimental investigation on heat transfer to supercritical CO_2 in a microtube up to 30 MPa for application in the NET power cycle, Appl. Therm. Eng. (2025) 129206, https://doi.org/10.1016/j.applthermaleng.2025.129206.

[52] W. Nusslet, Die oberflächenkondensation des Wasserdampfes, Z VDI 60 (1916) 541–546.

[53] J. Müller, Wärmeübergang bei der filmkondensation und seine einordnung in Wärme- und Stoffübertragungsvorgänge bei filmströmungen, Fortsch. Ber. VDI 3 (1992).

[54] Verein Deutscher Ingenieure, VDI Heat Atlas, Springer, Berlin Heidelberg, 2010, https://doi.org/10.1007/978-3-540-77877-6.

[55] Y.A. Cengel, J.M. Cimbala, Fluid mechanics: Fundamentals and Applications, 4th ed., McGraw-Hill Education, Columbus, OH, 2024.

[56] R. Numrich, Influence of gas flow on heat transfer in film condensation, Chem. Eng. Technol. 13 (1990) 136–143, https://doi.org/10.1002/ceat.270130119.

[57] R. Numrich, N. Claus, M. Hadley, Influence of gas flow on condensation process, Eurotherm. Seminar. Paris (1995), https://doi.org/10.1002/ceat.270130119.

[58] T.H. Chilton, A.P. Colburn, Mass transfer coefficients: prediction from data on heat transfer and fluid friction, Ind. Eng. Chem. (1934), https://doi.org/10.1021/ie50299a012.

[59] E.N. Fuller, K. Ensley, J.C. Giddings, Diffusion of halogenated hydrocarbons in helium. The effect of structure on collision cross sections, J. Phys. Chem. 73 (1969) 3679–3685, https://doi.org/10.1021/j100845a020.

[60] B.E. Poling, J.M. Prausnitz, J.P. O'Connell, Properties of Gases and Liquids, 5th edition, McGraw-Hill Education, New York, 2001.

[61] E. Romeo, C. Royo, A. Monzón, Improved explicit equations for estimation of the friction factor in rough and smooth pipes, Chem. Eng. J. 86 (2002) 369–374, https://doi.org/10.1016/S1385-8947(01)00254-6.

[62] G. Musgrove, S. Sullivan, D. Shiferaw, P. Fourspring, L. Chordia, Heat exchangers. Fundamentals and Applications of Supercritical Carbon Dioxide (SCO_2) Based Power Cycles, Elsevier, 2017, pp. 217–244, https://doi.org/10.1016/B978-0-08-100804-1.00008-6.

[63] The MathWorks Inc, MATLAB version: 9.13.0 (R2022b), (2022). https://www.mathworks.com (accessed June 12, 2023).

[64] J. Arrieta, R. Ferreira, Pardo, A. Rodríguez-Bernal, Análisis numérico de ecuaciones diferenciales ordinarias, Paraninfo, Madrid, 2020.

[65] X.L. Li, G.H. Tang, D.L. Yang, Y.H. Fan, J.L. Xu, Thermal-hydraulic-structural evaluation of S–CO_2 cooling wall tubes: a thermal stress evaluating criterion and optimization, Int. J. Therm. Sci. 170 (2021) 107161, https://doi.org/10.1016/j.ijthermalsci.2021.107161.

[66] K. Wang, P.S. Jia, Y. Zhang, Z.D. Zhang, T. Wang, C.H. Min, Thermal-fluid-mechanical analysis of tubular solar receiver panels using supercritical CO_2 as heat transfer fluid under non-uniform solar flux distribution, Sol. Energy 223 (2021) 72–86, https://doi.org/10.1016/j.solener.2021.05.030.